

STRUCTURED GENERATIVE MODELING WITH THE THERMODYNAMIC KOLMOGOROV-ARNOLD MODEL

Prithvi Raj

Zettascale Computing Co. *

prithvi@zettalaboratories.com

ABSTRACT

Learning an energy-based model (EBM) in the latent space of a top-down generative model offers an expressive and interpretable framework for text and image generation. However, it remains unclear how this interpretability can be used to guide model design, improve generative quality, and reduce training time. Moreover, the reliance on Langevin Monte Carlo (LMC) sampling presents challenges in efficiency and sampling multimodal latent distributions. In this work, we propose a novel adaptation of the Kolmogorov–Arnold representation theorem for generative modeling and introduce the Thermodynamic Kolmogorov–Arnold Model (T-KAM) to take advantage of structural and inductive biases. By constraining the prior to univariate relationships, T-KAM enables fast and exact inference via the inverse transform method. With the low dimensionality of the latent space and suitable inductive biases encoded, we demonstrate that importance sampling becomes a viable, unbiased, and highly efficient training strategy. We also introduce a training criterion using population-based LMC, which decomposes posterior sampling into a sequence of annealed distributions to improve multimodal exploration. T-KAM elegantly balances common trade-offs in generative modeling, offering fast inference, high sample quality, and stable training, while being naturally suited to upcoming Zettascale Computing Co. hardware and extendable to other high-impact research directions in generative intelligence.

1 INTRODUCTION

Deep generative modeling is a core subfield of machine learning that enables systems to learn complex data distributions, generate novel data, and support a wide range of tasks including simulation, compression, and representation learning. Two prominent and widely studied approaches are Variational Autoencoders (VAEs) (Kingma & Welling, 2022) and Generative Adversarial Networks (GANs) (Goodfellow et al., 2014). Both frameworks assume that each data point is generated from a low-dimensional latent vector via a top-down neural network, where the latent vector is typically drawn from a simple, non-informative prior, such as a uniform or isotropic Gaussian distribution.

Latent energy-based prior models (EBMs) (Pang et al., 2020) extend this framework by learning an expressive, data-dependent prior directly in the latent space. This prior can be trained jointly with the top-down generator using maximum likelihood estimation (MLE), where the EBM learns by the statistical discrepancy between samples from the prior and posterior distributions, following a paradigm similar to Empirical Bayes. Each learning iteration requires Markov Chain Monte Carlo (MCMC) sampling from both the prior and posterior, specifically the Unadjusted Langevin Algorithm (ULA) (Brooks et al., 2011; Rosicky et al., 1978b; Roberts & Stramer, 2002), which offers greater modeling flexibility compared to the amortized inference methods of VAEs.

Despite being extendable to several high-impact research directions, such as multimodal generative modeling (Yuan et al., 2024), and interpretable classification and meta-learning (Kong et al., 2021), (which involves rapid adaptability and few-shot generalization to out-of-distribution tasks), latent EBMs face critical limitations due to their reliance on MCMC sampling.

*Previously Exa Laboratories

Firstly, MCMC is inherently iterative, and algorithms such as ULA require repeated gradient evaluations through the model, introducing significant computational overhead during both training and inference. Secondly, ULA is best suited for sampling from smooth, unimodal distributions and tends to struggle when exploring the multimodal latent distributions that are typical in latent variable generative modeling. Moreover, separate ULA samplers are required for prior and posterior sampling, which is problematic given that ULA is sensitive to hyperparameter tuning: step sizes that are too small lead to poor mixing and convergence, while larger step sizes can accumulate discretization bias due to its use of the Euler–Maruyama method to evolve the underlying Langevin equation.

Additionally, it is not evident how the unique separation between the prior and generator networks can be leveraged for interpretability or training efficiency. Unlike the framework introduced by Karniadakis et al. (2021), which describes how scientific inductive and learning biases can be embedded into neural networks to reduce their reliance on data and improve training efficiency, generalization, and explainability, (all of which are critical for ensuring trust in Artificial Intelligence), it remains unclear how the EBM prior can be effectively aligned with the posterior to achieve similar effects. Although ideas from mechanistic interpretability, as reviewed by Bereska & Gavves (2024), could potentially be applied, there is currently no established method to leverage the unique strengths of the EBM prior framework for this purpose.

1.1 INDUCTIVE BIASES AND IMPORTANCE SAMPLING

To address these limitations, we reimagine the EBM prior framework into a novel univariate or element-wise model, drawing inspiration from Kolmogorov–Arnold Networks (KANs) (Liu et al., 2024) and deep spline networks Bohra et al. (2020), which replace the sigmoidal activations used in multilayer perceptrons Murtagh (1991) with spline interpolations. By representing the latent space with univariate functions and distributions, we improve interpretability for domain experts who may not be deeply familiar with computational statistics and machine learning.

This allows the EBM prior to be aligned with the posterior before training begins. We show that improved prior–posterior alignment enables efficient training with importance sampling (IS) (Goertzel, 1949), a technique for estimating posterior expectations that is otherwise avoided in the literature due to its degeneracy under severe prior–posterior mismatch and the curse of dimensionality, (Dupuis & Wang, 2004). Moreover, the trained prior can be visualized or recovered, offering new opportunities for transfer learning and scientific discovery.

This is tested in Sec. 3.1. Multiple KAN bases and reference priors are used to verify the effect of inductive bias. However, Gaussian Radial Basis Functions (RBF KANs) (Li, 2024), were used instead of the cubic B-spline bases proposed by Liu et al. (2024), as RBFs are more efficient for GPU implementation, and Poggio & Girosi (1990) previously demonstrated that they provide an optimal solution to the regularized approximation/interpolation problem.

To derive our new model, which we call the Thermodynamic Kolmogorov–Arnold Model (T-KAM), we first introduce a novel adaptation of the Kolmogorov–Arnold Representation Theorem (KART) (Givental et al., 2009) by reinterpreting its inner functions as Markov kernels between probability spaces. Given its finite and definitive nature, KART can provide structural bias and reduce the reliance of architecture design on heuristics and automated tuning. This reinterpretation allows us to frame inverse transform sampling (ITS) (Devroye, 1986) as a measurable transformation applied to uniform noise, thus preserving the deterministic structure of KART while admitting a probabilistic interpretation that aligns with MLE.

To address the potential inflexibility of strict adherence to KART and the limitations of using independent energy-based priors, we introduce a scalable strategy based on mixture distributions. Beyond introducing dependencies between latent dimensions to capture inter-dimensional relationships, this also improves sampling efficiency by enabling component-wise sampling.

1.2 POPULATION-BASED LANGEVIN SAMPLING AND THERMODYNAMIC TRAINING

However, while ITS enables fast inference, posterior sampling during training must still be conducted using ULA when the IS estimator is insufficient. Prior work addressing poor MCMC convergence and multimodal exploration in EBMs has typically relied on diffusion models, such as the hierarchical EBM by Cui & Han (2024) and the diffusion-assisted EBM by Zhang et al. (2023). To

maintain prior interpretability and fast inference post-training, we instead introduce posterior annealing as a novel and alternative strategy. This involves decomposing the posterior into a sequence of power posteriors, presented by Friel & Pettitt (2008), and sampling with population-based MCMC methods, specifically Parallel Tempering (PT) (Swendsen & Wang, 1986) (Swendsen & Wang, 1986; Marinari & Parisi, 1992; Hukushima & Nemoto, 1996).

Although this may reduce expressivity compared to hierarchical EBMs, it ensures that inductive biases remain easy to embed into the latent prior and interpret after training. Our training criterion is then derived from the discretized Thermodynamic Integral and the Steppingstone Estimator (SE), as presented by Calderhead & Girolami (2009); Annis et al. (2019) to ensure the impact of annealing on learning dynamics and parameter updates.

While ULA is computationally efficient and enables more flexible chain dynamics, it does not preserve detailed balance or reversibility. This can be recovered by incorporating Metropolis-Hastings (MH) adjustments (Metropolis & Ulam, 1949) via the Metropolis-adjusted Langevin Algorithm (MALA) (Rosky et al., 1978a). The codebase in Sec. A.1 optionally supports MALA with locally adaptive step-size tuning, (autoMALA) (Biron-Lattes et al., 2024), to assist when a single step size fails to accommodate the varying geometries of power posteriors, and when the MH criterion deteriorates under the curse of dimensionality, (Hairer et al., 2014).

MALA and autoMALA are discussed under Secs. A.6.3 and A.6.4. However, ULA remains the preferred method in our work, motivated by its demonstrated efficiency and effectiveness by Pang et al. (2020), and further supported by the findings of Nijkamp et al. (2019b;a), with regards to how short-run, biased MCMC methods can still be highly effective for sampling from EBMs.

These scaling strategies are compared in Sec. 3.2. Despite our optimizations, the element-wise and localized nature of KAN functions complicate their parallelization on GPUs, which are best suited to matrix arithmetic. As a result, forward passes through T-KAM and the gradient evaluations required for ULA were found to be slow, necessitating reduced experimental complexity.

We ultimately found that our mixture prior model outperformed a deep KAN prior architecture closely aligned with the model used in the study by Pang et al. (2020), while also offering greater computational efficiency. In contrast, the use of annealing could not be justified due to its significant computational overhead and limited gains in quality.

However, this assessment may change as a greater number of power posteriors and more sophisticated posterior sampling algorithms become feasible with the emerging hardware advances proposed by Zetta (2024). Their architecture enables fine-grained control over data flow and parallelized element-wise nonlinearity which is naturally well suited to supporting T-KAM at scale, while improving the potential of univariate priors with its function fusion features.

We present T-KAM as an initial step to inspire further adaptations of KART in machine learning. This work aims to lay the groundwork for more exploration amongst the research community, with the far-reaching hope of eventually advancing towards a broader conceptualization: *“The Kolmogorov-Arnold Representation Theorem Is All You Need.”*

2 THE THERMODYNAMIC KOLMOGOROV-ARNOLD MODEL

This section introduces the model and its associated sampling procedures. We begin by presenting a novel interpretation of the Kolmogorov–Arnold Representation Theorem (KART) to define the model’s baseline architecture. Our key practical contribution is the introduction of a univariate energy-based prior, detailed in Sec. 2.1. The top-down generator can be instantiated in various forms, including Kolmogorov–Arnold Networks (KANs), which enables strict adherence to KART.

We then propose scalable extensions to the model, including mixture distributions in Sec. 2.3.2, which introduce dependencies between latent dimensions. This represents a novel contribution to the literature on EBM priors. The final sections address prior and posterior sampling: we introduce inverse transform sampling (ITS) as a new approach for efficient EBM prior sampling, and introduce the posterior annealing strategy in Sec. 2.5 to improve multimodal sampling during training.

The Kolmogorov–Arnold Representation theorem (KART) (Givental et al., 2009) forms the basis of T-KAM. A structured proof of the theorem has been provided by Dzhenzher & Skopenkov (2022).

The Kolmogorov-Arnold Representation theorem 1 *For any integer $n_z > 1$, there are continuous univariate functions $\Phi_q : \mathbb{R} \rightarrow \mathbb{R}$ and $\psi_{q,p} : [0, 1] \rightarrow \mathbb{R}$, such that any continuous multivariate function, $g : [0, 1]^{n_z} \rightarrow \mathbb{R}$, can be represented as a superposition of those functions:*

$$g(u_1, \dots, u_{n_z}) = \sum_{q=1}^{2n_z+1} \Phi_q \left(\sum_{p=1}^{n_z} \psi_{q,p}(u_p) \right), \quad (1)$$

Eq. 1 can provide structural bias and guide the design of T-KAM’s architecture. To ensure adherence to it, any transformations must be derived to be continuous, measurable, and deterministic. For readers less familiar with the technical background, the two most practically significant equations of Sec.. 2.1 are Eqs. 4 & 6.

2.1 UNIVARIATE ENERGY-BASED PRIOR

We interpret $u_p \sim \mathcal{U}(u_p; 0, 1)$ in Eq. 1 as a uniform random variable in the probability space, $([0, 1], \mathcal{B}([0, 1]), \mu)$, where $\mathcal{B}([0, 1])$ is the Borel σ -algebra on $[0, 1]$ and μ is the Lebesgue measure on $[0, 1]$. To ensure that the transformation $u_p \mapsto \psi_{q,p}(u_p)$ is well defined in a probabilistic setting, we require it to be a Markov kernel. For all Borel measurable sets $A \subseteq \mathcal{Z}$, where $\mathcal{Z} \subset \mathbb{R}$ is introduced as the latent space of T-KAM, the map

$$u_p \mapsto K(u_p, A) = \delta_{\psi_{q,p}(u_p)}(A) \quad (2)$$

is measurable. Here, $\delta_{\psi_{q,p}(u_p)}$ denotes the Dirac measure centred at $\psi_{q,p}(u_p)$, ensuring the kernel is deterministic: i.e., once u_p is sampled, the outcome in \mathcal{Z} is fixed. This measurability requirement guarantees that the pushforward from $([0, 1], \mathcal{B}([0, 1]), \mu)$ to $(\mathcal{Z}, \mathcal{B}(\mathcal{Z}), \pi)$ is well defined and that no additional stochasticity is introduced beyond the uniform source variable, u_p . Here, $\mathcal{B}(\mathcal{Z})$ is the Borel σ -algebra on the latent space, \mathcal{Z} , and π is the latent measure.

The functions $\psi_{q,p}$ can therefore be conveniently interpreted as inverse cumulative distribution functions (CDFs) corresponding to independent univariate priors:

$$\psi_{q,p}(u_p) = F^{-1}(\pi_{q,p})(u_p). \quad (3)$$

Here, $F^{-1}(\pi_{q,p}) : [0, 1] \rightarrow \mathcal{Z}$ is the generalized inverse CDF associated with a parameterized latent distribution, $\pi_{q,p}$. This is valid under standard regularity assumptions on F , since it is a measurable, monotone, increasing function, and thus $F^{-1}(u) = \inf \{z \in \mathcal{Z} : F(z) \geq u\}$ is a measurable mapping between the two probability spaces. We parameterize the latent distribution $\pi_{q,p}$ via exponential tilting of a base prior π_0 :

$$\pi_{q,p}(z) = \frac{\exp(f_{q,p}(z))}{Z_{q,p}} \pi_0(z), \quad (4)$$

where $f_{q,p}(z)$ is a learned energy function and $Z_{q,p}$ is the normalizing constant (partition function) that ensures $\pi_{q,p}$ defines a valid probability. The inspiration for this exponential tilting form can be traced to the energy-based prior introduced by Pang et al. (2020), adapted to the univariate case. The base prior π_0 serves as a reference measure that guides the form of the learned distribution $\pi_{q,p}$, allowing for flexible reweighting via the energy function $f_{q,p}$.

For $\pi_{q,p}$ to define a valid probability distribution, it must satisfy countable additivity while being non-negative and normalized. This is guaranteed since $f_{q,p} : \mathcal{Z} \rightarrow \mathbb{R}$ is Borel-measurable and integrable with respect to the reference density π_0 , ensuring the finiteness of the partition function:

$$Z_{q,p} = \int_{\mathcal{Z}} \exp(f_{q,p}(z)) d\pi_0(z) < \infty. \quad (5)$$

In practice, $f_{q,p}$ can be parameterized in various ways, made possible by the recent development of Kolmogorov–Arnold Networks (KANs) (Liu et al., 2024). For instance, smoothing splines, such as those used by KANs or deep spline networks, (Bohra et al., 2020). Splines are typically defined on bounded domains, allowing the support of $\pi_{q,p}$ to be explicitly controlled by the user.

The partition function $Z_{q,p}$ is often intractable in energy-based models. However, in this univariate setting, where the energy function is smooth and defined on a bounded domain $[z_{\min}, z_{\max}]$, it can be

accurately approximated using Gauss–Kronrod quadrature, (Laurie, 1997):

$$Z_{q,p} = \int_{z_{\min}}^{z_{\max}} \exp(f_{q,p}(z))\pi_0(z)dz \approx \sum_{i=1}^{N_{\text{quad}}} w_i G(z_i^{\text{node}}), \quad (6)$$

where $G(z) = \exp(f_{q,p}(z))\pi_0(z)$, and $\{z_i^{\text{node}}, w_i\}_{i=1}^{N_{\text{quad}}}$ are the quadrature nodes and weights for the interval $[z_{\min}, z_{\max}]$. The smoothness of G , together with its bounded support, makes this approximation highly accurate.

With an valid form for the normalized CDF, inverse transform sampling (ITS) can be used to draw samples from $\pi_{q,p}$ as deterministic transformations of uniform noise. This preserves the deterministic structure of KART while enabling flexible, learnable latent distributions. Inverse transform sampling remains effective even for functions that are not Riemann integrable, provided they are integrable in the Lebesgue sense, typical for the functions in KAN literature.

As a result, the model retains a coherent probabilistic interpretation of KART that is consistent with the energy-based framework proposed by Pang et al. (2020), which is well suited to maximum likelihood training. However, this approach is significantly limited, as it ignores inter-dimensional dependencies in the latent space and results in an axis-aligned joint distribution. We address this inflexibility in Sec. 2.3.2 by relaxing our adherence to KART.

2.2 KOLMOGOROV-ARNOLD NETWORK GENERATOR

Having sampled the intermediary latent variable with ITS such that $z_{q,p} = F^{-1}(\pi_{q,p})(u_p)$, the generator can be realized flexibly as $\mathcal{G} : \mathcal{Z} \rightarrow \mathcal{X}$:

$$\tilde{\mathbf{x}}^{(s)} = \mathcal{G}\left(\mathbf{z}^{(s)}\right) + \boldsymbol{\epsilon}^{(s)}, \quad \text{where } z_{q,p}^{(s)} \sim \pi_{q,p}(z), \quad \boldsymbol{\epsilon}^{(s)} \sim \mathcal{N}(\boldsymbol{\epsilon}; \mathbf{0}, \sigma_\epsilon^2 \mathbf{I}), \quad (7)$$

where $\tilde{\mathbf{x}}^{(s)} = \{\tilde{x}_o^{(s)}\}_{o=1}^{n_x}$ represents a generated data sample corresponding to a single latent sample indexed by s , and n_x is used to specify the dimension of $\tilde{\mathbf{x}}^{(s)}$. The additive noise is a Gaussian sample with hyperparameter σ_ϵ . However, the architecture may be made strictly adherent to KART using a Kolmogorov-Arnold Network:

$$\tilde{x}_o^{(s)} = \sum_{q=1}^{2n_z+1} \Phi_{o,q} \left(\sum_{p=1}^{n_z} z_{q,p}^{(s)} \right) + \epsilon_o^{(s)}, \quad \tilde{\mathbf{x}}^{(s)} = \begin{pmatrix} \sum_{q=1}^{2n_z+1} \Phi_{1,q} \left(\sum_{p=1}^{n_z} z_{q,p}^{(s)} \right) \\ \sum_{q=1}^{2n_z+1} \Phi_{2,q} \left(\sum_{p=1}^{n_z} z_{q,p}^{(s)} \right) \\ \vdots \\ \sum_{q=1}^{2n_z+1} \Phi_{n_x,q} \left(\sum_{p=1}^{n_z} z_{q,p}^{(s)} \right) \end{pmatrix} + \boldsymbol{\epsilon}^{(s)}. \quad (8)$$

The functions, $\Phi_{o,q} : \mathbb{R} \rightarrow \mathbb{R}$, are realizable as basis or KAN functions similar to $f_{q,p} : \mathcal{Z} \rightarrow \mathbb{R}$.

2.3 SCALING T-KAM

The trainable components of the prior and inner functions are shared across the features of each input $\mathbf{x}^{(b)}$, while the outer generator functions remain separate for each output dimension. Specifically, the learnable functions are defined as:

$$\mathbf{f} = \begin{pmatrix} (f_{1,1}, \dots, f_{1,n_z}) \\ (f_{2,1}, \dots, f_{2,n_z}) \\ \vdots \\ (f_{2n_z+1,1}, \dots, f_{2n_z+1,n_z}) \end{pmatrix}, \quad \boldsymbol{\Phi} = \begin{pmatrix} (\Phi_{1,1}, \dots, \Phi_{1,2n_z+1}) \\ (\Phi_{2,1}, \dots, \Phi_{2,2n_z+1}) \\ \vdots \\ (\Phi_{n_x,1}, \dots, \Phi_{n_x,2n_z+1}) \end{pmatrix}, \quad (9)$$

where n_x denotes the dimensionality of the observed data.

From this point forward, we formulate our derivations over a multivariate probability space $(\mathcal{Z}, \mathcal{B}(\mathcal{Z}), P)$, where \mathcal{Z} no longer represents a subinterval of the real line, but rather a subspace of $\mathbb{R}^{(2n_z+1) \times n_z}$. The measure P defines a product distribution over the latent variables:

$$P(\mathbf{z} | \mathbf{f}) = \pi_{1,1} \otimes \dots \otimes \pi_{2n_z+1,n_z},$$

where each component $\pi_{j,k}$ is defined via exponential tilting, as introduced in Sec. 2.1. The full latent vector \mathbf{z} is a matrix-valued random variable composed of the independent latent features.

2.3.1 GENERATOR

The generator, \mathcal{G} , can be considered a separate generator network allowing for more flexible realizations, such as convolutional layers when adherence to Eq. 1 is not required. Deepening this generator, as guided by Liu et al. (2024) for the Kolmogorov-Arnold Network (KAN), does not replace KART as the innermost foundation of T-KAM:

$$x_o^{(s)} = \sum_{l_n=1}^{L_n} h_{o,l_n} \left(\dots h_{l_3,l_2} \left(\sum_{l_1=1}^{L_1} h_{l_2,l_1} \left(\sum_{q=1}^{2n_z+1} \Phi_{l_1,q} \left(\sum_{p=1}^{n_z} z_{q,p}^{(s)} \right) \right) \right) \right) + \epsilon_o^{(s)}. \quad (10)$$

Here, each h represents a hidden layer introduced between the outer sum of Eq. 1, and the output feature space to allow for more expressivity when required. In fact, each successive instance of h can be interpreted as a distinct outer sum of Eq. 1, where the inner sum corresponds to the previous layer. This is valid provided that:

$$L_1 = 2(2n_z + 1) + 1, \quad L_2 = 2L_1 + 1, \quad \dots \quad L_n = 2L_{n-1} + 1. \quad (11)$$

Thus, a smooth transition between the latent space and data space can be achieved by progressively doubling layer widths, eliminating the need for arbitrary choices while maintaining relaxed compliance with KART. Strict adherence to KART can be achieved for hidden layer $h_{l_k,l_{k-1}}$ by applying either a sigmoid or affine transformation after layer $h_{l_{k-2},l_{k-3}}$ to shift its range back to $[0, 1]^{L_{k-1}}$. However, using sigmoid may lead to vanishing gradients and we contend that function domains are less critical to KART than its structural properties and should not be prioritized over maintaining gradient flow and avoiding saturation.

Adopting a KAN-based generator also allows for training with L1 regularization, followed by pruning with the method proposed by Liu et al. (2024). This enables further model compression beyond the baseline structure defined by KART.

2.3.2 MIXTURE PRIOR

As noted in Sec. 2.1, the independence of the priors $\pi_{q,p}$ limits expressivity. Moreover, the summation over p in Eq. 8 accumulates the variances of sampled $z_{q,p}$, which can lead to overly diffuse representations. To address this, particularly for more complex generative tasks such as those in Sec. 3.2, we relax the strict adherence to KART by reformulating the prior as a mixture distribution. This involves moving the summation over p out of the generator and absorbing it into the prior, yielding a mixture model:

$$\sum_{p=1}^{n_z} \pi_{q,p}(z) = \sum_{p=1}^{n_z} \alpha_{q,p} \frac{\exp(f_{q,p}(z))}{Z_{q,p}} \pi_0(z), \quad \text{where} \quad \sum_{p=1}^{n_z} \alpha_{q,p} = 1, \quad \alpha_{q,p} \geq 0. \quad (12)$$

Here, $\alpha_{q,p}$ denote mixture weights, practically enforced via a softmax function. The resulting distribution defines a mixture of energy-based priors. Sampling becomes more efficient than in the previous formulation, as it proceeds component-wise using ITS for discrete variables, (Devroye, 2006). However, this violates adherence to KART, since F now corresponds to a discrete rather than continuous CDF.

To encourage balanced weighting and reduce model complexity, L1 regularization can be applied to $\alpha_{q,p}$ and small values can be pruned. The mixture proportions are learned by adding $\log \alpha_{q,p}$ to the gradients of the prior in Sec. 2.4.1. Component selection follows a categorical distribution over $p = 1, \dots, n_z$, determined by $\alpha_{q,p}$. Let $u_{\text{mix}} \sim \mathcal{U}(u_{\text{mix}}; 0, 1)$. Guided by Devroye (2006) regarding how ITS applied to discrete variables, the selected component p^* is given by:

$$p^* = \min \left\{ j \mid \sum_{p=1}^j \alpha_{q,p} \geq u_{\text{mix}} \right\}. \quad (13)$$

This ensures that each component p^* is selected with probability α_{q,p^*} . ITS can then be used to sample from the chosen component, (see 2.4.3).

2.3.3 DEEP KAN PRIOR

If required, we may further deepen the energy functions $f_{q,p}$ using the KAN approach. In fact, each $f_{q,p}$ can itself be a realization of Eq. 1 when its domain is restricted to $[0, 1]$. This extension introduces new challenges:

1. Prior interpretability is reduced, complicating the recovery of trained priors.
2. The component-wise structure is compromised, undermining the validity of ITS and KART.

Instead, we propose removing the summation over p in Eq. 8 and reparameterizing the prior using a multilayer KAN energy function, which can be deepened as needed:

$$P(\mathbf{z} | \mathbf{f}) = \frac{1}{\mathcal{Z}} \cdot \exp \left(\sum_{q=1}^{2n_z+1} \Psi_{q,p} \left(\sum_{p=1}^{n_z} f_{q,p}(z) \right) \right) \cdot \pi_0(\mathbf{z}), \quad (14)$$

where $\mathbf{z} \in \mathcal{Z} \subset \mathbb{R}^{n_z}$, and is constrained to $[0, 1]^{n_z}$ when strict adherence to KART is required. Sampling from this prior can be carried out using the Unadjusted Langevin Algorithm (ULA), as described in Sec. 2.5.2.

2.4 MAXIMUM LIKELIHOOD TRAINING

With N_x training examples in a batch, the optimization objective is the minimization of the negative log-marginal likelihood:

$$\min_{\mathbf{f}, \Phi} \mathcal{L}(\mathbf{x}^{(1)}, \dots, \mathbf{x}^{(N_x)}) = \min_{\mathbf{f}, \Phi} \left[- \sum_{b=1}^{N_x} \log \left(P(\mathbf{x}^{(b)} | \mathbf{f}, \Phi) \right) \right]. \quad (15)$$

The conditional dependency on the collection, \mathbf{f}, Φ , represents all learnable elements of T-KAM. For each sample of $\mathbf{x}^{(b)}$, the log-marginal likelihood in Eq. 15 can be separated out into two log-distributions by first introducing the latent vector, \mathbf{z} , otherwise absent upon marginalization over the latent distribution. This is shown under Sec. A.4.2, and the resulting expectation exhibits a lack of dependence on sampling, as proven under Sec. A.4.3:

$$\nabla_{\mathbf{f}, \Phi} \left[\log P(\mathbf{x}^{(b)} | \mathbf{f}, \Phi) \right] = \mathbb{E}_{P(\mathbf{z} | \mathbf{x}^{(b)}, \mathbf{f}, \Phi)} \left[\nabla_{\mathbf{f}} [\log P(\mathbf{z} | \mathbf{f})] + \nabla_{\Phi} \left[\log P(\mathbf{x}^{(b)} | \mathbf{z}, \Phi) \right] \right], \quad (16)$$

2.4.1 LOG-PRIOR

Given the independence of the prior’s parameters, the log-prior can be modeled as a sum over the univariate cases:

$$\log \left(P(\mathbf{z} | \mathbf{f}) \right) = \sum_{q=1}^{2n_z+1} \sum_{p=1}^{n_z} \log (\pi_{q,p}(z_{q,p})) = \sum_{q=1}^{2n_z+1} \sum_{p=1}^{n_z} f_{q,p}(z_{q,p}) + \log (\pi_0(z_{q,p})) - \log (Z_{q,p}) \quad (17)$$

Tractable normalization is available through Eq. 6, however it may be more efficient to discard normalization in the learning gradient. In Sec. A.4.4, we derive the contrastive divergence learning gradient for T-KAM, which is faster to train and more typical of energy-based modeling:

$$\begin{aligned} \mathbb{E}_{P(\mathbf{z} | \mathbf{x}, \mathbf{f}, \Phi)} \left[\nabla_{\mathbf{f}} [\log P(\mathbf{z} | \mathbf{f})] \right] &= \mathbb{E}_{P(\mathbf{z} | \mathbf{x}, \mathbf{f}, \Phi)} \left[\nabla_{\mathbf{f}} \sum_{q=1}^{2n_z+1} \sum_{p=1}^{n_z} f_{q,p}(z_{q,p}) \right] \\ &\quad - \mathbb{E}_{P(\mathbf{z} | \mathbf{f})} \left[\nabla_{\mathbf{f}} \sum_{q=1}^{2n_z+1} \sum_{p=1}^{n_z} f_{q,p}(z_{q,p}) \right]. \end{aligned} \quad (18)$$

Here, \mathbf{z} is sampled from $P(\mathbf{z} | \mathbf{f})$ and $P(\mathbf{z} | \mathbf{x}^{(b)}, \mathbf{f}, \Phi)$ and reflects a univariate element of the prior model. The expectation with respect to the posterior can be approximated using Importance

Sampling (IS), outlined under Secs. 2.4.4 & A.6.1, or a standard Monte Carlo estimator when using Langevin sampling methods. The prior expectation may always be approximated with a Monte Carlo estimator taken across samples:

$$\mathbb{E}_{P(z|f)} \left[\nabla_{\mathbf{f}} \sum_{q=1}^{2n_z+1} \sum_{p=1}^{n_z} f_{q,p}(z_{q,p}) \right] \approx \frac{1}{N_s} \sum_{s=1}^{N_s} \nabla_{\mathbf{f}} \sum_{q=1}^{2n_z+1} \sum_{p=1}^{n_z} f_{q,p}(z_{q,p}) \quad \text{where } z_{q,p}^{(s)} \sim \pi_{q,p}(z). \quad (19)$$

The gradient of Eq. 18 can therefore be viewed as a element-wise correction to the prior, incorporating information from the observations to align the prior with the posterior, thereby following the philosophy of empirical Bayes. The gradient can then be evaluated via autodifferentiation.

2.4.2 LOG-LIKELIHOOD

Depending on the task the log-likelihood can be modeled in multiple ways. For example, a Gaussian model might be adopted for images, and an autoregressive model for text. It can also be realized into a multimodal generative modeling framework using the principles outlined by Yuan et al. (2024).

$$\log \left(P \left(\mathbf{x}^{(b)} \mid \mathbf{z}, \Phi \right) \right) = \begin{cases} -\frac{\|\mathbf{x}^{(b)} - \tilde{\mathbf{x}}\|_2^2}{2\sigma_{\text{llhood}}^2} + \text{const}, & \text{(static continuous data)} \\ \sum_{o=1}^{n_x} \sum_{c=1}^K x_{o,c}^{(b)} \log \tilde{x}_{o,c} + \text{const}, & \text{(static discrete data)} \\ \sum_{t=1}^T \log \left(P \left(\mathbf{x}^{(b,t)} \mid \mathbf{x}^{(b,1)}, \dots, \mathbf{x}^{(b,t-1)}, \mathbf{z}, \Phi \right) \right), & \text{(sequential data)} \end{cases} \quad (20)$$

Here, $\tilde{\mathbf{x}}$ is a generated sample from Eq. 8 corresponding to a single batch item, $\mathbf{x}^{(b)}$, σ_{llhood} is a hyperparameter subject to assumptions regarding the variance of the data, and K denotes the number of discrete classes. The learning gradient attributed to the log-likelihood can also be evaluated using autodifferentiation, after first approximating the posterior expectation with IS or MC estimators.

2.4.3 PRIOR INVERSE TRANSFORM SAMPLING

In Eqs. 8 & 19, $z_{q,p}$ is drawn from $\pi_{q,p}$ with inverse transform sampling, (ITS) (Devroye, 1986). ITS can be used to sample from a component of the latent distribution, $\pi_{q,p}$, made possible given the unique characteristics of T-KAM. Specifically, the univariate, finite-grid structure of the constituent functions enables quadrature/interpolating integral approximations.

1. **CDF inversion:** Sampling occurs using the inverse cumulative distribution function (CDF): The CDF for a single component, $F_{\pi_{q,p}}$, is:

$$F_{\pi_{q,p}}(z') = \frac{\int_{z_{\min}}^{z'} \exp(f_{q,p}(z)) \pi_0(z) dz}{Z_{q,p}}, \quad Z_{q,p} = \int_{z_{\min}}^{z_{\max}} \exp(f_{q,p}(z)) \pi_0(z) dz. \quad (21)$$

These two integrals can be conveniently and efficiently approximated using Gauss-Kronrod quadrature, (Laurie, 1997), given that $f_{q,p}$ is univariate and defined on a bounded grid:

$$G(z) = \exp(f_{q,p}(z)) \pi_0(z), \quad \int_{z_{\min}}^{z'} G(z) dz \approx \sum_{i=1}^{N_{\text{quad}}} w_i G(z_i^{\text{node}}), \quad (22)$$

where z_i^{node} and w_i are the Gauss-Legendre quadrature nodes and weights for the interval $[z_{\min}, z']$. A random variable is uniformly drawn and shared across q , $u_p \sim \mathcal{U}(u_p; 0, 1)$. The first interval where $F_{\pi_{q,p}}(z)$ is greater than u_p scaled by $Z_{q,p}$ is identified:

$$k^* = \min \left\{ j \mid \sum_{i=1}^j w_i G(z_i^{\text{node}}) \geq Z_{q,p} \cdot u_p \right\}. \quad (23)$$

2. **Linear interpolation:** The sample z_p is interpolated within the subset, $[z_{k^*-1}^{\text{node}}, z_{k^*}^{\text{node}}]$:

$$z_p \approx z_{k^*-1}^{\text{node}} + (z_{k^*}^{\text{node}} - z_{k^*-1}^{\text{node}}) \cdot \frac{u_p - F_{\pi_{q,p}}(z_{k^*-1}^{\text{node}})}{F_{\pi_{q,p}}(z_{k^*}^{\text{node}}) - F_{\pi_{q,p}}(z_{k^*-1}^{\text{node}})}. \quad (24)$$

The procedure ensures an efficient, exact and unbiased generation of samples, $z_{q,p}$, distributed according to $\pi_{q,p}$. It can be vectorized to generate samples from all prior elements.

2.4.4 POSTERIOR EXPECTATIONS WITH IMPORTANCE SAMPLING

The log-marginal likelihood and its learning gradient presented in Eqs. 15 & 16, involve expectations with respect to the posterior $P(\mathbf{z} | \mathbf{x}^{(b)}, \mathbf{f}, \Phi)$, which is potentially multimodal and complex. We propose Importance Sampling (IS) (Goertzel, 1949) as an efficient method for estimating its expectation when prior task knowledge can be incorporated into the model to improve prior-posterior alignment and the quality of the IS estimator.

IS provides a quick approximation of the posterior expectation without requiring extensive exploration. In contrast, ULA, (introduced in Sec. 2.5.2) is more stochastic and exploratory, often yielding higher-quality samples from the posterior, when the prior is poorly matched.

The following procedure is elaborated in more detail under Sec. A.6.1:

1. **Proposal distribution:** N_s independent samples, $\{\mathbf{z}^{(s)}\}_{s=1}^{N_s}$, are drawn from the proposal distribution, $Q(\mathbf{z}) = P(\mathbf{z} | \mathbf{f})$, which the target distribution, $P(\mathbf{z} | \mathbf{x}^{(b)}, \mathbf{f}, \Phi)$ must be absolutely continuous with respect to. Sampling from Q is tractable with the procedure outlined in Sec. 2.4.3.

2. **Importance weights:** The normalized importance weights are evaluated:

$$w_{\text{norm}}(\mathbf{z}^{(s)}) = \frac{w(\mathbf{z}^{(s)})}{\sum_{r=1}^{N_s} w(\mathbf{z}^{(r)})} = \text{softmax}_s \left(\log(P(\mathbf{x}^{(b)} | \mathbf{z}^{(s)}, \Phi)) \right). \quad (25)$$

3. **Effective Sample Size:** To prevent weight degeneracy, resampling is conducted when the Effective Sample Size (ESS) falls below a threshold specified by a hyperparameter, γ :

$$ESS = \frac{1}{\sum_{s=1}^{N_s} w_{\text{norm}}(\mathbf{z}^{(s)})} < \gamma \cdot N_s. \quad (26)$$

Otherwise, the weights are taken without alteration, (i.e. the next step is skipped). When the weights are uniformly spread the ESS evaluates to N_s . High-variance weights with a low ESS indicate that many samples contribute minimally, resulting in inefficient sampling. Resampling focuses learning on samples that are more representative of the posterior distribution, thereby maximizing the usefulness of each parameter update.

4. **Resample:** If required, the population, $\{\mathbf{z}^{(s)}, w_{\text{norm}}(\mathbf{z}^{(s)})\}_{s=1}^{N_s}$, is resampled from. There are multiple ways to accomplish this, (Douc et al., 2005). Systematic, stratified, and residual resampling are provided in the codebase under Sec. A.1, parallelized on the CPU. In this study, we adopted residual resampling, (explained under Sec. A.6.2).
5. **Expectation estimation:** The posterior expectation of an arbitrary function $\rho(\mathbf{z})$, (e.g., the log-likelihood), is estimated with a Monte Carlo estimator:

$$\mathbb{E}_{P(\mathbf{z} | \mathbf{x}^{(b)}, \mathbf{f}, \Phi)}[\rho(\mathbf{z})] \approx \sum_{s=1}^{N_s} \rho(\mathbf{z}_{\text{resampled}}^{(s)}) \cdot w_{\text{norm}}(\mathbf{z}_{\text{resampled}}^{(s)}). \quad (27)$$

This estimator is used for computing the log-marginal likelihood and its gradient in Eqs. 15 and 16. However, unlike ULA (discussed in Sec. 2.5.2 and demonstrated in Sec. 3.2), IS fails to support posterior exploration when the prior is poorly aligned, making it unsuitable for general-purpose tasks beyond those similar to the datasets presented in Secs. 3.1.

2.5 POPULATION-BASED AND LANGEVIN MONTE CARLO POSTERIOR SAMPLING

To mitigate the poor convergence of multimodal ULA sampling, we introduce a training criterion that facilitates posterior annealing. Details on the cyclic annealing schedule adopted in this study, along with practical guidance on hyperparameter selection, are provided in Sec. A.3.

2.5.1 THERMODYNAMIC TRAINING CRITERION

We inform our derivations using the Thermodynamic Integral. In place of the log-marginal likelihood outlined in Eq. 15, this exploits the following representation derived in Sec. A.4.5:

$$\log \left(P(\mathbf{x}^{(b)} | \mathbf{f}, \Phi) \right) = \int_0^1 \mathbb{E}_{P(\mathbf{z} | \mathbf{x}^{(b)}, \mathbf{f}, \Phi, t)} \left[\log \left(P(\mathbf{x}^{(b)} | \mathbf{z}, \Phi) \right) \right] dt \quad (28)$$

Here, $P(z | \mathbf{x}^{(b)}, \mathbf{f}, \Phi, t)$ has been introduced as the power posterior, which can be considered a representation of the original posterior distribution, with a likelihood tempered by a temperature parameter, t . This is introduced by Friel & Pettitt (2008) and organized for our purposes as follows:

$$P(z | \mathbf{x}^{(b)}, \mathbf{f}, \Phi, t) = \frac{P(\mathbf{x}^{(b)} | z, \Phi)^t \cdot P(z | \mathbf{f})}{Z_t},$$

$$\text{where } Z_t = \mathbb{E}_{P(z|\mathbf{f})} \left[P(\mathbf{x}^{(b)} | z, \Phi)^t \right] = \int_{\mathcal{Z}} P(\mathbf{x}^{(b)} | z, \Phi)^t dP(z | \mathbf{f}) \quad (29)$$

Given the form of Eq. 29, setting $t = 0$ results in the power posterior distribution assuming the form of the prior distribution. As t increments, the posterior gradually adopts a shape more closely resembling the true Bayesian posterior measure. At $t = 1$, the posterior recovers its original form and converges to the original posterior distribution.

The effect of tempering is illustrated in Fig. 1, starting with a Gaussian prior that is entirely un-informed of $\mathbf{x}^{(b)}$. As t increases from 0 to 1, the contribution of the likelihood term in Eq. 29 progressively grows, ultimately leading to the posterior at $t = 1$. This final posterior can be interpreted as the prior updated by information from the samples of $\mathbf{x}^{(b)}$.

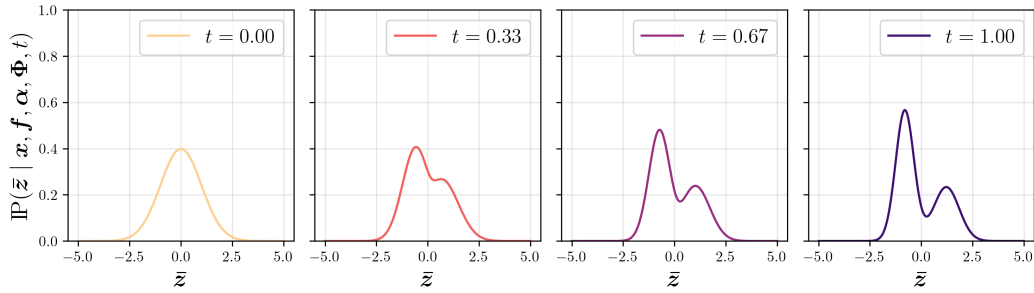


Figure 1: Demonstration of power posterior evolution with t . A simple Gaussian prior is sculpted into forms that resemble a more complex, multi-modal posterior as t is incremented from 0 to 1.

The exact calculation of the integral in Eq. 28 is feasible given that the bounds are $t = 0$, corresponding to the expectation being taken with respect to the prior, and $t = 1$, where it is taken with respect to the posterior. However, the integral can also be expressed exactly without collapsing the temperatures, offering greater flexibility in how the integral evolves through the temperature schedule, $\{t_k\}_{k=0}^{N_t}$. In particular, the temperature schedule is discretized as:

$$\mathbf{t} = (t_0, t_1, \dots, t_{N_t}), \quad t_k \in [0, 1] \quad (30)$$

In Sec. A.4.7, the Steppingstone estimator (SE) introduced by Annis et al. (2019) is derived from the discretized Thermodynamic Integral presented by Calderhead & Girolami (2009), (and provided under Sec. A.4.6). This establishes a connection between the two, which we use to derive the learning gradient and inform our approach to the clustering the temperatures in Eq. 30:

$$\log \left(P(\mathbf{x}^{(b)} | \mathbf{f}, \Phi) \right) = \sum_{k=1}^{N_t} \log \left(\frac{Z_{t_k}}{Z_{t_{k-1}}} \right) = \sum_{k=1}^{N_t} \left(\log(Z_{t_k}) - \log(Z_{t_{k-1}}) \right) = \underbrace{\log(Z_{t_{N_t}})}_{=\text{MLE}} - \underbrace{\log(Z_{t_0})}_{=0 \text{ (Eq. 38)}}. \quad (31)$$

The log-partition ratios are estimated with Monte Carlo estimators using all annealed samples:

$$\begin{aligned} \log \left(P(\mathbf{x}^{(b)} | \mathbf{f}, \Phi) \right) &= \log(Z_{t_{N_t}})^{\text{SS}} = \sum_{k=1}^{N_t} \log \left(\frac{Z_{t_k}}{Z_{t_{k-1}}} \right) \\ &\approx \frac{1}{N_s} \sum_{k=1}^{N_t-1} \sum_{s=1}^{N_s} (t_{k+1} - t_k) \left[\log P \left(\mathbf{x}^{(b)} | \mathbf{z}^{(s, t_k)}, \Phi \right) \right], \quad \text{where } \underbrace{\mathbf{z}^{(s, t_k)} \sim P(z | \mathbf{x}^{(b)}, \mathbf{f}, \Phi, t_k)}_{\text{Sec.2.5.2}} \end{aligned} \quad (32)$$

SE and its variants, such as Annealed Importance Sampling (AIS) (Neal, 1998), are commonly used to estimate a model’s evidence without a tractable way to learn the prior, as they lack dependence on prior gradients beyond sampling. However, by recognizing the direct connection between the SE and MLE learning gradients, as proven in Sec. A.4.7, one can simply add the contrastive divergence learning gradient from Eq. 18 to the SE estimator.

This is valid because the SE gradient matches the MLE gradient, and the likelihood gradient is independent of the prior gradient. The posterior expectation of contrastive divergence in Eq. 18 can be estimated with a Monte Carlo estimator using the final samples of ULA.

2.5.2 UNADJUSTED LANGEVIN ALGORITHM (ULA) AND REPLICA EXCHANGE

In their implementation of Thermodynamic Integration, Calderhead & Girolami (2009) estimated the Thermodynamic Integral using the discretization in Sec. A.4.6, using population-based MCMC and Parallel Tempering (PT) (Swendsen & Wang, 1986; Marinari & Parisi, 1992; Hukushima & Nemoto, 1996) to simultaneously sample from all power posteriors.

Specifically, parallel chains were maintained at each temperature, (or Replica), using Metropolis-Hastings (MH) (Metropolis & Ulam, 1949), to drive local moves for each power posterior. They also proposed a geometric path between the prior and posterior, enabling global swaps between adjacent temperatures. This approach allowed higher temperatures to leverage the efficient mixing of lower temperatures, thereby facilitating a more thorough exploration of the posterior landscape.

We adopt a similar strategy but follow Pang et al. (2020) in using the Unadjusted Langevin Algorithm (ULA) (Rossky et al., 1978b; Brooks et al., 2011) without MH correction. Specifically, we update samples using the forward Euler–Maruyama discretization of the Langevin SDE, as detailed by Roberts & Stramer (2002), with the transition kernel described in Sec. A.6.3:

$$\mathbf{z}^{(i+1, t_k)} = \mathbf{z}^{(i, t_k)} + \eta \nabla_{\mathbf{z}^{(i, t_k)}} \log \gamma \left(\mathbf{z}^{(i, t_k)} \right) + \sqrt{2\eta} \boldsymbol{\epsilon}^{(i, t_k)}, \quad (33)$$

where η is the step size, $\boldsymbol{\epsilon}^{(i, t_k)} \sim \mathcal{N}(\mathbf{0}, \mathbf{I})$, and γ_{t_k} denotes the target power posterior:

$$\log \gamma \left(\mathbf{z}^{(i, t_k)} \right) = \log P(\mathbf{z}^{(i, t_k)} \mid \mathbf{x}^{(b)}, \mathbf{f}, \Phi, t_k) \propto t_k \log P(\mathbf{x}^{(b)} \mid \mathbf{z}^{(i, t_k)}, \Phi) + \log P(\mathbf{z}^{(i, t_k)} \mid \mathbf{f}).$$

ULA is best suited for smooth, unimodal distributions, but annealing with power posteriors might improve sampling from multimodal distributions. Mixing can be further improved by periodically swapping populations between randomly selected adjacent temperatures, subject to:

$$r = \frac{P(\mathbf{x}^{(b)} \mid \mathbf{z}^{(i, t_{k+1})}, \Phi)^{t_k} P(\mathbf{x}^{(b)} \mid \mathbf{z}^{(i, t_k)}, \Phi)^{t_{k+1}}}{P(\mathbf{x}^{(b)} \mid \mathbf{z}^{(i, t_k)}, \Phi)^{t_k} P(\mathbf{x}^{(b)} \mid \mathbf{z}^{(i, t_{k+1})}, \Phi)^{t_{k+1}}}, \quad (34)$$

where the proposed swap, $\mathbf{z}^{(i, t_{k+1})} \leftrightarrow \mathbf{z}^{(i, t_k)}$, is accepted with probability: $\min(1, r)$.

3 EXPERIMENTS

Our experiments are designed to highlight the unique advantages of T-KAM and to compare the proposed strategies for scaling and training. In Sec. 3.1, we demonstrate the effects of introducing different inductive biases through the choice of reference distributions in Eq. 4, as well as through the KAN basis functions used for $f_{q,p}$ and $\Phi_{o,q}$ with comparisons between Radial Basis Functions (RBFs) (Li, 2024) and Fourier bases (FFTs) (Xu et al., 2024). We show that, when appropriate biases are encoded, importance sampling becomes a viable and highly efficient training strategy. We also demonstrate that the model remains effective when strictly adhering to KART with independent energy-based priors, thereby validating the use of KART as a source of structural inductive bias.

In Sec. 3.2, we compare the mixture EBM prior sampled using ITS against a deep EBM prior sampled using ULA. The latter shares an architectural design similar to that used by Pang et al. (2020), but with Chebyshev KAN (SS et al., 2024) energy functions. We further compare T-KAM trained using single-posterior ULA sampling with the MLE criterion against a population-based ULA sampling strategy using the SE criterion. These comparisons serve to evaluate the practical

strategies proposed for scaling and training T-KAM, as well as to compare ITS and our mixture EBM against ULA and deep EBMs, previously used by Pang et al. (2020).

To quantify the fidelity of generated data in a more reliable manner than previous studies in the literature, we used effectively unbiased metrics based on the principles outlined by Chong & Forsyth (2020). By applying linear regression to extrapolate the values of standard metrics to an infinitely sized sample set, Monte Carlo error was mitigated, (otherwise associated with finite sample sizes).

For Sec. 3.2, we gathered $\overline{\text{FID}}_\infty$ and $\overline{\text{KID}}_\infty$, which are effectively unbiased estimators of the Fréchet Inception Distance and Kernel Inception Distance, introduced by Heusel et al. (2018); Bińkowski et al. (2021) respectively. The set of sample sizes used for the linear regression were: 1000, 1200, 1400, 1600, 1800, 2000, 2200, 2400, 2600, 2800, 3000.

However, we recognise that quantifying the fidelity of generated data is inherently challenging and not an exact science. While the metrics used in this study have limitations, they align with those commonly found in the literature. Our conclusions are also informed by our subjective perception of the images. Furthermore, no metrics were applied in Secs. 3.1.1 & 3.1.1, as vision metrics rely on the Inception V3 model trained on ImageNet (Szegedy et al., 2015), potentially introducing bias against other datasets.

More image samples are provided in Sec. A.7.

3.1 INDUCTIVE BIASES ENABLE IMPORTANCE SAMPLING

3.1.1 MNIST & FMNIST

The MNIST (Deng, 2012) and FMNIST (Xiao et al., 2017) datasets are grayscale datasets that can be modeled with the first likelihood model from Eq. 20. The first collection of benchmarks presented in Sec. A.2 were obtained using the hyperparameters and architecture specified for this experiment in Tab. 4. T-KAM was trained for 10 epochs with 20,000 training examples, an importance sample size of $N_s = 100$, and a batch size of $N_x = 100$, (corresponding to 2,000 parameter updates) Prior sampling was conducted with ITS and posterior expectations were estimated with IS. The architecture was guided by KART and independent priors were used.

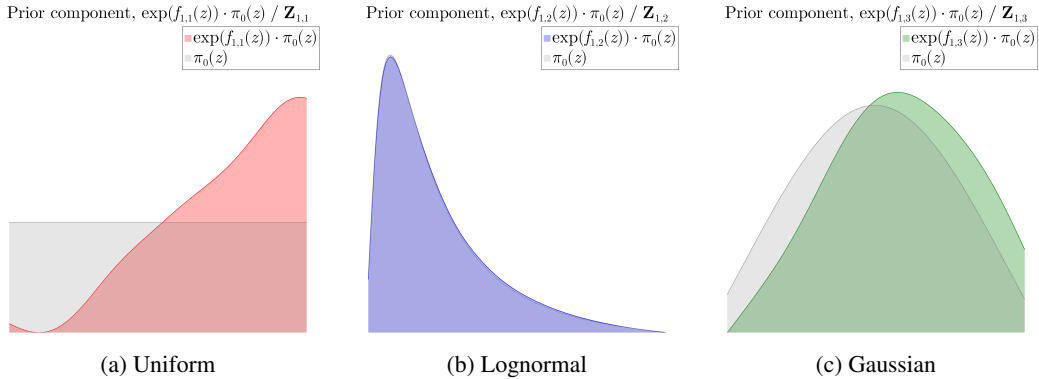


Figure 2: Exponentially-tilted priors, extracted after training on MNIST with RBFs. These plots illustrate how T-KAM can be visualized and interpreted by how its priors are adjusted relative to their reference distributions. The lognormal prior remains untrained due to posterior collapse, while the uniform prior has been skewed towards $z_{1,2} = 1$. Gaussian is only slightly tilted.

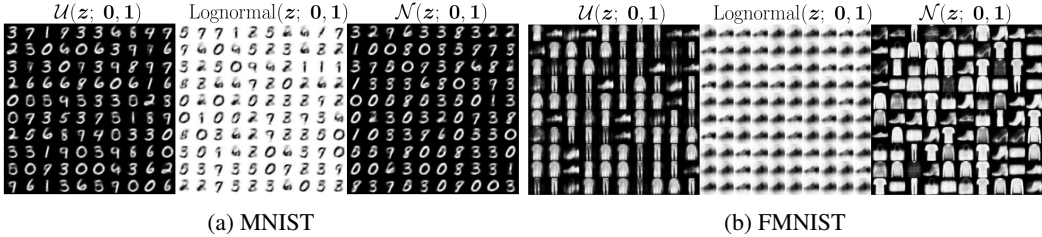


Figure 3: Generated NIST images using RBFs and different exponentially-tilted priors, initialized from $\mathcal{N}(z; \mathbf{0}, \mathbf{1})$, $\text{Lognormal}(z; \mathbf{0}, \mathbf{1})$, and $\mathcal{U}(z; \mathbf{0}, \mathbf{1})$. Lognormal is inverted for clarity.

Lognormal priors resulted in posterior mode collapse. T-KAM learned to generate an average of all MNIST or FMNIST classes, and failed to learn a meaningful latent prior. In contrast, Gaussian priors produced the sharpest images for FMNIST, and uniform yielded the sharpest MNIST digits.

In Fig. 2, we show how T-KAM allows visualization of its univariate latent distributions, which is an interpretability advantage that can help us explain the observed results. Unlike Gaussian and uniform reference distributions, which provide a more symmetric and balanced initial spread over the latent space, lognormal priors introduce a strong right-skew. This asymmetric initialization makes it difficult for T-KAM to learn flexible, separable representations, ultimately impairing its ability to produce binary output features.

In contrast, the symmetric nature of Gaussian and uniform priors allows the sculpting of latent distributions and their skews to support binary generation. When cross-referencing with the priors of other latent features plotted in Sec. A.8, it becomes evident that left-skewed distributions are more successful at MNIST and FMNIST generation. This explains why the standard lognormal prior, which is right-skewed, is poorly suited to these datasets.

The experiment also demonstrates the validity of importance sampling for posterior expectations when prior-posterior alignment can be improved by choosing an appropriate reference prior, since uniform and Gaussian priors produced realistic MNIST and FMNIST samples respectively.

3.1.2 2D DARCY FLOW PRESSURES

The dataset used in this experiment was sourced from Li et al. (2021). The Darcy flow equation is a second-order elliptic partial differential equation (PDE) that models various physical phenomena, including fluid flow through porous media and heat conduction. At steady state, its two-dimensional form on the unit square with Dirichlet boundary conditions is given by:

$$\begin{aligned}
 -\nabla \cdot (k(\mathbf{z}), \nabla u(\mathbf{z})) &= f(\mathbf{z}), & \mathbf{z} &\in [0, 1]^2, \\
 u(\mathbf{z}) &= 0, & \mathbf{z} &\in \partial[0, 1]^2,
 \end{aligned}
 \tag{35}$$

where $k(\mathbf{z})$ is the 2D permeability field, $u(\mathbf{z})$ represents the 2D pressure field, and $f(\mathbf{z})$ is a forcing function evaluated at \mathbf{z} . Generating new flow-pressure samples is a challenging task in machine learning. One approach is to use input permeability samples while employing the Fourier Neural Operator (FNO) (Li et al., 2021), to learn the solution operator mapping between permeability and flow pressure. However, in this study, we use the purely generative task to illustrate how weak inductive biases can influence what T-KAM learns.

T-KAM was trained to generate new Darcy flow pressures using a batch size and importance sample size of $N_x = 50, N_s = 50$. The training usespanned 600 epochs with 1,000 training examples, resulting in 12,000 parameter updates. All other hyperparameters are provided in Tab. 5. Prior sampling was conducted with ITS and posterior expectations were estimated with IS. The architecture was guided by KART and independent priors were used.

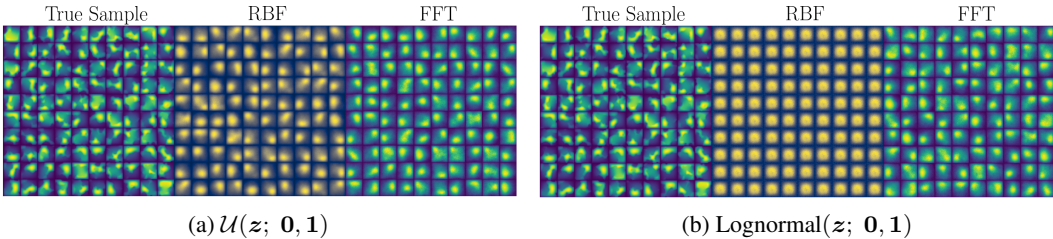


Figure 4: Generated Darcy flow pressures with exponentially-tilted priors initialized from standard uniform and lognormal distributions. RBF bases, are contrasted against FFT bases, where RBF is colored differently for clarity.

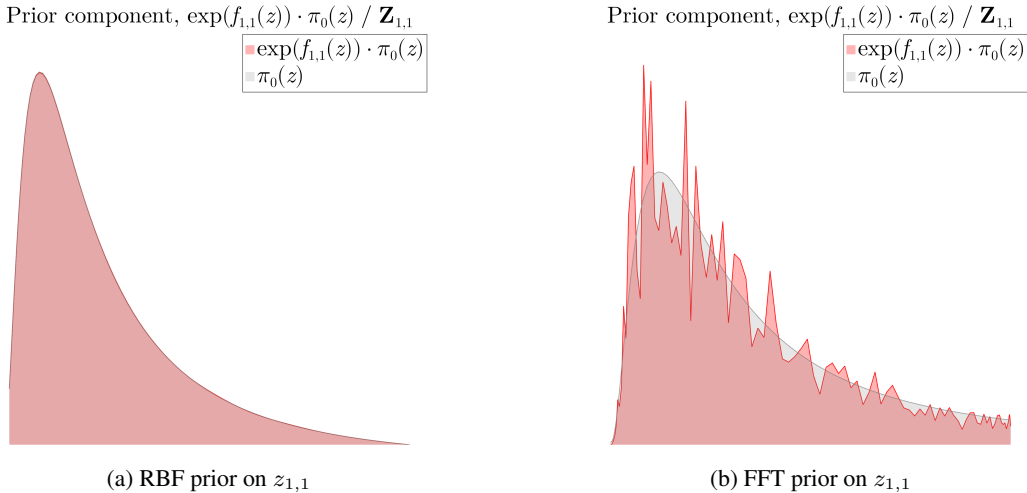


Figure 5: Comparison of exponentially-tilted lognormal priors, extracted after training on Darcy between RBF bases and FFT bases. RBF basis functions led to oversmoothing and posterior collapse, while FFT bases lacked smoothness, potentially compromising adherence to the continuous assumptions imposed by KART.

Although RBFs tended to oversmooth the solution space, FFTs were more effective at capturing large-scale spatial periodicity. In cases where the prior was misspecified with a lognormal reference, RBFs failed to produce coherent samples, while FFTs still yielded coherent outputs.

This result likely stems from their suitability in representing periodic spatial relationships, a property that aligns well with the structure of the Darcy flow, as previously showcased by the success of the FNO, which also uses Fourier methods. This is somewhat reflected by Fig. 5b, which depicts some periodicity in the learned, exponentially-tilted distribution on $z_{1,1}$. However, FFT-parameterized energy functions were also found to be non-smooth and potentially discontinuous, which is also illustrated by the distribution plotted in Fig. 5b. This might have compromised adherence to KART and future work might explore incorporating regularization to improve their smoothness.

This shows that the choice of basis functions serves as an additional mechanism for encoding inductive bias, complementing the role of the reference prior. Once again, importance sampling proved to be viable when appropriate inductive biases were encoded.

3.2 COMPARING SCALING STRATEGIES AGAINST CIFAR-10 & SVHN

T-KAM, when adherent to KART, can be interpreted as a dense or spline-based network. However, for spatial data, convolutional neural networks (CNNs) (LeCun et al., 2015), are more suitable as the generator, \mathcal{G} . In addition to their computational efficiency through weight sharing, CNNs offer

a key advantage over dense networks due to their spatial inductive bias: sequences of convolutional layers implement shift-equivariant transformations that are well-suited for images.

Due to limited computational resources during this study, (detailed in Sec. A.2), training was shortened from 70,000 to 8,000 parameter updates. Given their parameter efficiency, Chebyshev bases (SS et al., 2024) were used for the prior energy functions. The deep prior architecture mirrored that of Pang et al. (2020), but it is important to note that dense KANs do not directly replicate the behavior of standard dense layers. Additionally, we used a single optimizer to train both models, rather than using separate optimizers for the prior and generator networks. We considered these discrepancies to be acceptable, given the comparative nature of this experiment.

Posterior sampling was conducted with ULA, and a Gaussian reference was used, $\pi_0 = \mathcal{N}(z; \mathbf{0}, \mathbf{1})$. T-KAM was trained for 20 epochs with a batch size of $N_x = 100$ on 40,000 training examples. All remaining hyperparameters are provided in Tab. 6, and architectural details for the mixture and deep prior models, as well as the CNN generators, are included in Sec. A.5.1. Annealing was conducted with $N_t = 5$ power posteriors and the cyclic temperature scheduling outlined in Sec. A.3.1.

For brevity, only the SVHN images are visualized in the main body. Samples of CIFAR-10 are provided under Sec. A.7.5

Table 1: Effectively unbiased FID and KID scores (lower is better) for SVHN.

Prior	MLE	SE
Mixture	$\overline{\text{FID}}_\infty = 81.02$	$\overline{\text{FID}}_\infty = 82.13$
	$\overline{\text{KID}}_\infty = 0.0669$	$\overline{\text{KID}}_\infty = 0.0673$
Deep	$\overline{\text{FID}}_\infty = 107.42$	$\overline{\text{FID}}_\infty = 141.24$
	$\overline{\text{KID}}_\infty = 0.0970$	$\overline{\text{KID}}_\infty = 0.1320$

Table 2: Effectively unbiased FID and KID scores (lower is better) for CIFAR-10.

Prior	MLE	SE
Mixture	$\overline{\text{FID}}_\infty = 159.11$	$\overline{\text{FID}}_\infty = 180.00$
	$\overline{\text{KID}}_\infty = 0.1600$	$\overline{\text{KID}}_\infty = 0.1858$
Deep	$\overline{\text{FID}}_\infty = 185.10$	$\overline{\text{FID}}_\infty = 201.75$
	$\overline{\text{KID}}_\infty = 0.1780$	$\overline{\text{KID}}_\infty = 0.1977$



(a) SVHN with mixture prior and MLE



(b) SVHN with mixture prior and SE



(a) SVHN with deep prior and MLE



(b) SVHN with deep prior and SE

Figure 6: Generated samples from T-KAM trained on SVHN using a mixture prior.

Figure 7: Generated samples from T-KAM trained on SVHN using a deep prior.

The mixture prior with ITS outperformed the deep prior with ULA, while also being more computationally efficient and enabling faster inference, (Tab. 9). This advantage is likely due to ITS providing exact samples from the prior, whereas ULA produces only approximate, biased samples.

SE did not outperform MLE and cannot be justified in this setting given its computational overhead. Alternative approaches, such as different annealing schedules or the use of autoMALA with bias correction and temperature-adaptive step size tuning, could improve performance, but they are not worth investigating until the hardware of Zetta (2024) becomes available, due to the added complexity, hyperparameter tuning, and extended training time.

The results confirm the superiority of mixture EBMs paired with ITS over deep EBMs sampled with ULA as a viable approach to scaling. However, the advantages of SE and population-based ULA remain inconclusive.

4 CONCLUSIONS

T-KAM provides a principled and scalable framework for structured and informed generative modeling. Our results demonstrate that incorporating inductive biases through both basis functions and reference priors can enable more efficient training strategies, such as importance sampling. We also show how the Kolmogorov–Arnold representation theorem can inform architectural design and introduce structural bias. Additionally, we find that the inverse transform method offers clear advantages over Langevin Monte Carlo sampling for energy-based priors. While mixture priors with inverse transform sampling consistently outperformed alternative approaches across both datasets, the benefits of annealing and population-based MCMC remain inconclusive, suggesting directions for further work. Future investigations into the practicality of our annealing methods depend on continued hardware advancements, such as those introduced by Zetta (2024).

4.1 FUTURE WORK

4.1.1 HARDWARE ACCELERATION

Computational benchmarks are provided in Sec. A.2. The univariate and localized nature of spline interpolations complicates their parallelization on GPUs, since they involve sparse or recursive computations. Additionally, the search operations in Eqs. 13, 23, and 70 were parallelized on the CPU across samples, despite the remainder of T-KAM being executed on the GPU. This design stems from the fact that GPUs are generally ill-suited for parallelized search algorithms, which often rely on conditional logic. Parallelizing conditionals can lead to thread divergence, making CPUs more efficient for these operations.

While ITS enables fast inference and scales when the prior is a mixture model, T-KAM’s training with ULA does not scale efficiently on GPUs due to the iterative, gradient-based nature of ULA. Nonetheless, the unique advantages of T-KAM justify continued research and development. Notably, Zetta (2024) introduces the Learnable Function Unit (LFU), a processor designed for efficient evaluation and differentiation of univariate, nonlinear functions in parallel, while offering precise data flow control and high throughput.

The LFU presents a promising avenue for more efficient implementations of ULA, and improved posterior sampling, potentially including bias correction and adaptive step size tuning with autoMALA, (Sec. A.6.4). Even without annealing, replacing ULA with autoMALA may yield a more robust probabilistic model with stronger theoretical guarantees.

Overall, T-KAM may prove more scalable than conventional generative models, owing to its reliance on finite representations of continuous functions and its compatibility with the LFU.

4.1.2 TEXT-TO-TEXT, CLASSIFICATION, AND MULTI-MODAL GENERATION

Kong et al. (2021) provided a robust framework for high-quality text-to-text generation, classification, and meta-learning, while Yuan et al. (2024) demonstrated how T-KAM might be adapted into a multi-modal generative model. This holds promise for future investigations and industry adoption, especially when the LFU becomes available. However, the symbol-vector coupling approach of Kong et al. (2021) must first be adapted to remain compatible with ITS.

4.1.3 IMPROVED SAMPLING FOR MULTIMODAL DISTRIBUTIONS

Despite its theoretical guarantees, annealing is difficult to justify given its computational cost and limited practical benefit. Future work could explore adaptations of the hierarchical EBMs proposed by Cui & Han (2024), without sacrificing the interpretability or efficiency of our model.

REFERENCES

Jeffrey Annis, Nathan J. Evans, Brent J. Miller, and Thomas J. Palmeri. Thermodynamic integration and steppingstone sampling methods for estimating bayes factors: A tutorial. *Journal of Mathematical Psychology*, 89:67–86, April 2019. doi: 10.1016/j.jmp.2019.01.005. URL <https://osf.io/jpnb4>. Epub 2019 Feb 13.

- Leonard Bereska and Efstratios Gavves. Mechanistic interpretability for ai safety – a review, 2024. URL <https://arxiv.org/abs/2404.14082>.
- Mikołaj Bińkowski, Danica J. Sutherland, Michael Arbel, and Arthur Gretton. Demystifying mmd gans, 2021.
- Miguel Biron-Lattes, Nikola Surjanovic, Saifuddin Syed, Trevor Campbell, and Alexandre Bouchard-Côté. automala: Locally adaptive metropolis-adjusted langevin algorithm, 2024. URL <https://arxiv.org/abs/2310.16782>.
- Pakshal Bohra, Joaquim Campos, Harshit Gupta, Shayan Aziznejad, and Michael Unser. Learning activation functions in deep (spline) neural networks. *IEEE Open Journal of Signal Processing*, 1:295–309, 2020. doi: 10.1109/OJSP.2020.3039379.
- Steve Brooks, Andrew Gelman, Galin Jones, and Xiao-Li Meng. *Handbook of Markov Chain Monte Carlo*. Chapman and Hall/CRC, May 2011. ISBN 9780429138508. doi: 10.1201/b10905. URL <http://dx.doi.org/10.1201/b10905>.
- Ben Calderhead and Mark Girolami. Estimating bayes factors via thermodynamic integration and population mcmc. *Computational Statistics & Data Analysis*, 53(12):4028–4045, 2009. ISSN 0167-9473. doi: <https://doi.org/10.1016/j.csda.2009.07.025>. URL <https://www.sciencedirect.com/science/article/pii/S0167947309002722>.
- Min Jin Chong and David Forsyth. Effectively unbiased fid and inception score and where to find them, 2020.
- Jiali Cui and Tian Han. Learning latent space hierarchical ebm diffusion models, 2024. URL <https://arxiv.org/abs/2405.13910>.
- Li Deng. The mnist database of handwritten digit images for machine learning research. *IEEE Signal Processing Magazine*, 29(6):141–142, 2012.
- Luc Devroye. *Non-Uniform Random Variate Generation*. Springer-Verlag, New York, 1986. ISBN 0-387-96305-7.
- Luc Devroye. Chapter 4 nonuniform random variate generation. In Shane G. Henderson and Barry L. Nelson (eds.), *Simulation*, volume 13 of *Handbooks in Operations Research and Management Science*, pp. 83–121. Elsevier, 2006. doi: [https://doi.org/10.1016/S0927-0507\(06\)13004-2](https://doi.org/10.1016/S0927-0507(06)13004-2). URL <https://www.sciencedirect.com/science/article/pii/S0927050706130042>.
- Randal Douc, Olivier Cappé, and Eric Moulines. Comparison of resampling schemes for particle filtering, 2005. URL <https://arxiv.org/abs/cs/0507025>.
- Simon Duane, A.D. Kennedy, Brian J. Pendleton, and Duncan Roweth. Hybrid monte carlo. *Physics Letters B*, 195(2):216–222, 1987. ISSN 0370-2693. doi: [https://doi.org/10.1016/0370-2693\(87\)91197-X](https://doi.org/10.1016/0370-2693(87)91197-X). URL <https://www.sciencedirect.com/science/article/pii/037026938791197X>.
- Paul Dupuis and Hui Wang. Importance sampling, large deviations, and differential games. *Stochastics and Stochastic Reports*, 76:481–508, 2004.
- S. Dzhenezher and A. Skopenkov. A structured proof of kolmogorov’s superposition theorem, 2022. URL <https://arxiv.org/abs/2105.00408>.
- N. Friel and A. N. Pettitt. Marginal likelihood estimation via power posteriors. *Journal of the Royal Statistical Society. Series B (Statistical Methodology)*, 70(3):589–607, 2008. ISSN 13697412, 14679868. URL <http://www.jstor.org/stable/20203843>.
- Hao Fu, Chunyuan Li, Xiaodong Liu, Jianfeng Gao, Asli Celikyilmaz, and Lawrence Carin. Cyclical annealing schedule: A simple approach to mitigating kl vanishing, 2019. URL <https://arxiv.org/abs/1903.10145>.

- Alexander B. Givental, Boris A. Khesin, Jerrold E. Marsden, Alexander N. Varchenko, Victor A. Vassiliev, Oleg Ya. Viro, and Vladimir M. Zakalyukin (eds.). *On the representation of functions of several variables as a superposition of functions of a smaller number of variables*, pp. 25–46. Springer Berlin Heidelberg, Berlin, Heidelberg, 2009. ISBN 978-3-642-01742-1. doi: 10.1007/978-3-642-01742-1_5. URL https://doi.org/10.1007/978-3-642-01742-1_5.
- Gerald Goertzel. Quota sampling and importance functions in stochastic solution of particle problems. Technical Report AECD-2793, U.S. Atomic Energy Commission, 1949. Technical Report, June 21, 1949.
- Ian J. Goodfellow, Jean Pouget-Abadie, Mehdi Mirza, Bing Xu, David Warde-Farley, Sherjil Ozair, Aaron Courville, and Yoshua Bengio. Generative adversarial networks, 2014. URL <https://arxiv.org/abs/1406.2661>.
- Martin Hairer, Andrew M. Stuart, and Sebastian J. Vollmer. Spectral gaps for a metropolis–hastings algorithm in infinite dimensions. *The Annals of Applied Probability*, 24(6), December 2014. ISSN 1050-5164. doi: 10.1214/13-aap982. URL <http://dx.doi.org/10.1214/13-AAP982>.
- W. K. Hastings. Monte carlo sampling methods using markov chains and their applications. *Biometrika*, 57(1):97–109, 04 1970. ISSN 0006-3444. doi: 10.1093/biomet/57.1.97. URL <https://doi.org/10.1093/biomet/57.1.97>.
- Martin Heusel, Hubert Ramsauer, Thomas Unterthiner, Bernhard Nessler, and Sepp Hochreiter. Gans trained by a two time-scale update rule converge to a local nash equilibrium, 2018.
- Koji Hukushima and Koji Nemoto. Exchange monte carlo method and application to spin glass simulations. *Journal of the Physical Society of Japan*, 65(6):1604–1608, June 1996. ISSN 1347-4073. doi: 10.1143/jpsj.65.1604. URL <http://dx.doi.org/10.1143/JPSJ.65.1604>.
- JuliaCI. `Benchmarktools.jl`, 2024. URL <https://juliaci.github.io/BenchmarkTools.jl/stable/>. Accessed on August 20, 2024.
- George Em Karniadakis, Ioannis G. Kevrekidis, Lu Lu, Paris Perdikaris, Sifan Wang, and Liu Yang. Physics-informed machine learning. *Nature Reviews Physics*, 3(6):422–440, 2021. ISSN 2522-5820. doi: 10.1038/s42254-021-00314-5. URL <https://doi.org/10.1038/s42254-021-00314-5>.
- Diederik P. Kingma and Max Welling. Auto-encoding variational bayes, 2022. URL <https://arxiv.org/abs/1312.6114>. arXiv:1312.6114.
- T. Kloek and H. K. van Dijk. Bayesian estimates of equation system parameters: An application of integration by monte carlo. *Econometrica*, 46(1):1–19, 1978. ISSN 00129682, 14680262. URL <http://www.jstor.org/stable/1913641>.
- Deqian Kong, Bo Pang, and Ying Nian Wu. Unsupervised meta-learning via latent space energy-based model of symbol vector coupling. In *Fifth Workshop on Meta-Learning at the Conference on Neural Information Processing Systems*, 2021. URL <https://openreview.net/forum?id=-pLftu7EpXz>.
- R. Larson and B.H. Edwards. *Calculus of a Single Variable*. Cengage Learning, 2008. ISBN 9780547209982. URL https://books.google.co.uk/books?id=gR7nGg5_9xcC.
- Dirk Laurie. Calculation of gauss-kronrod quadrature rules. *Math. Comput.*, 66:1133–1145, 07 1997. doi: 10.1090/S0025-5718-97-00861-2.
- Yann LeCun, Yoshua Bengio, and Geoffrey Hinton. Deep learning. *Nature*, 521(7553):436–444, May 28 2015. ISSN 1476-4687. doi: 10.1038/nature14539.
- Ziyao Li. Kolmogorov-arnold networks are radial basis function networks, 2024. URL <https://arxiv.org/abs/2405.06721>.
- Zongyi Li, Nikola Kovachki, Kamyar Aizzadenesheli, Burigede Liu, Kaushik Bhattacharya, Andrew Stuart, and Anima Anandkumar. Fourier neural operator for parametric partial differential equations, 2021. URL <https://arxiv.org/abs/2010.08895>.

- Ziming Liu, Yixuan Wang, Sachin Vaidya, Fabian Ruehle, James Halverson, Marin Soljačić, Thomas Y. Hou, and Max Tegmark. Kan: Kolmogorov-arnold networks, 2024. URL <https://arxiv.org/abs/2404.19756>.
- E. Marinari and G. Parisi. Simulated tempering: A new monte carlo scheme. *Europhysics Letters*, 19(6):451, jul 1992. doi: 10.1209/0295-5075/19/6/002. URL <https://dx.doi.org/10.1209/0295-5075/19/6/002>.
- Nicholas Metropolis and S. Ulam. The monte carlo method. *Journal of the American Statistical Association*, 44(247):335–341, 1949. ISSN 01621459, 1537274X. URL <http://www.jstor.org/stable/2280232>.
- Fionn Murtagh. Multilayer perceptrons for classification and regression. *Neurocomputing*, 2(5):183–197, 1991. ISSN 0925-2312. doi: [https://doi.org/10.1016/0925-2312\(91\)90023-5](https://doi.org/10.1016/0925-2312(91)90023-5). URL <https://www.sciencedirect.com/science/article/pii/0925231291900235>.
- Radford M. Neal. Annealed importance sampling, 1998. URL <https://arxiv.org/abs/physics/9803008>.
- Erik Nijkamp, Mitch Hill, Tian Han, Song-Chun Zhu, and Ying Nian Wu. On the anatomy of mcmc-based maximum likelihood learning of energy-based models, 2019a. URL <https://arxiv.org/abs/1903.12370>.
- Erik Nijkamp, Mitch Hill, Song-Chun Zhu, and Ying Nian Wu. Learning non-convergent non-persistent short-run mcmc toward energy-based model, 2019b. URL <https://arxiv.org/abs/1904.09770>.
- Bo Pang, Tian Han, Erik Nijkamp, Song-Chun Zhu, and Ying Nian Wu. Learning latent space energy-based prior model, 2020. URL <https://arxiv.org/abs/2006.08205>.
- T. Poggio and F. Girosi. Networks for approximation and learning. *Proceedings of the IEEE*, 78(9):1481–1497, 1990. doi: 10.1109/5.58326. URL <https://doi.org/10.1109/5.58326>.
- G. O. Roberts and O. Stramer. Langevin diffusions and metropolis-hastings algorithms. *Methodology and Computing in Applied Probability*, 4(4):337–357, 2002. ISSN 1573-7713. doi: 10.1023/A:1023562417138. URL <https://doi.org/10.1023/A:1023562417138>.
- P. J. Rossky, J. D. Doll, and H. L. Friedman. Brownian dynamics as smart monte carlo simulation. *The Journal of Chemical Physics*, 69(10):4628–4633, 11 1978a. ISSN 0021-9606. doi: 10.1063/1.436415. URL <https://doi.org/10.1063/1.436415>.
- P. J. Rossky, J. D. Doll, and H. L. Friedman. Brownian dynamics as smart monte carlo simulation. *The Journal of Chemical Physics*, 69(10):4628–4633, 1978b. doi: 10.1063/1.436415.
- Sidharth SS, Keerthana AR, Gokul R, and Anas KP. Chebyshev polynomial-based kolmogorov-arnold networks: An efficient architecture for nonlinear function approximation, 2024. URL <https://arxiv.org/abs/2405.07200>.
- Robert Swendsen and Jian-Sheng Wang. Replica monte carlo simulation of spin-glasses. *Physical review letters*, 57:2607–2609, 12 1986. doi: 10.1103/PhysRevLett.57.2607.
- Christian Szegedy, Vincent Vanhoucke, Sergey Ioffe, Jonathon Shlens, and Zbigniew Wojna. Re-thinking the inception architecture for computer vision, 2015.
- Han Xiao, Kashif Rasul, and Roland Vollgraf. Fashion-mnist: a novel image dataset for benchmarking machine learning algorithms, 2017. URL <https://arxiv.org/abs/1708.07747>.
- Jinfeng Xu, Zheyu Chen, Jinze Li, Shuo Yang, Wei Wang, Xiping Hu, and Edith C. H. Ngai. Fourierkan-gcf: Fourier kolmogorov-arnold network – an effective and efficient feature transformation for graph collaborative filtering, 2024. URL <https://arxiv.org/abs/2406.01034>.

Shiyu Yuan, Jiali Cui, Hanao Li, and Tian Han. Learning multimodal latent generative models with energy-based prior, 2024. URL <https://arxiv.org/abs/2409.19862>.

Zetta. Zetta, the next paradigm of sustainable computing. <https://zettalaboratories.com/litepaper>, August 2024. Zetta introduces a polymorphic computing chip technology, achieving up to 27.6x efficiency gains over the H100 GPUs through dynamically reconfigurable hardware that adapts to diverse AI models via software configuration.

Xinwei Zhang, Zhiqiang Tan, and Zhijian Ou. Persistently trained, diffusion-assisted energy-based models, 2023. URL <https://arxiv.org/abs/2304.10707>.

Song Chun Zhu and D. Mumford. Grade: Gibbs reaction and diffusion equations. In *Sixth International Conference on Computer Vision (IEEE Cat. No.98CH36271)*, pp. 847–854, 1998. doi: 10.1109/ICCV.1998.710816.

A APPENDIX

A.1 CODEBASE

The study was implemented at <https://github.com/eva-laboratories/T-KAM>.

A.2 COMPUTATIONAL BENCHMARKS

These benchmarks were collected for FP32 on a GPU (NVIDIA GeForce GTX 1650) with Julia’s BenchmarkTools package, (JuliaCI, 2024). The index search operations in Eqs. 23, 13, & 70 were parallelized across 12 threads on a CPU (i7-9750H @ 2.60GHz).

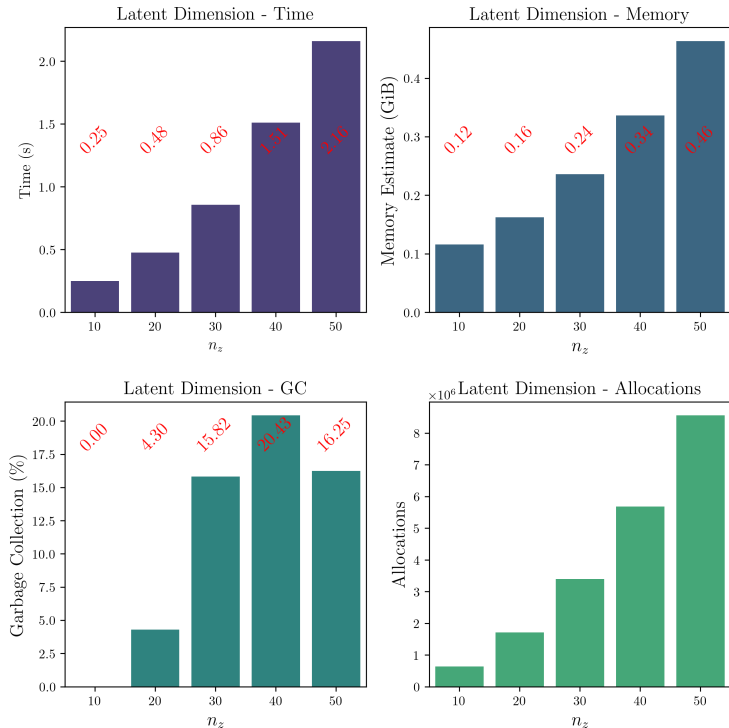


Figure 8: Benchmarks for varying latent dimensions, n_z , while sampling from independent EBM priors with ITS and estimating posterior expectations with IS. The prior had an input size of n_z and an output size of $2n_z + 1$. The generator received inputs of size $2n_z + 1$, with a hidden size of $4n_z + 2$ and an output size of 28×28 . All other hyperparameters were kept consistent with Tab. 4. They reflect the performance of a reverse autodifferentiation of the MLE criterion, Eq. 16.

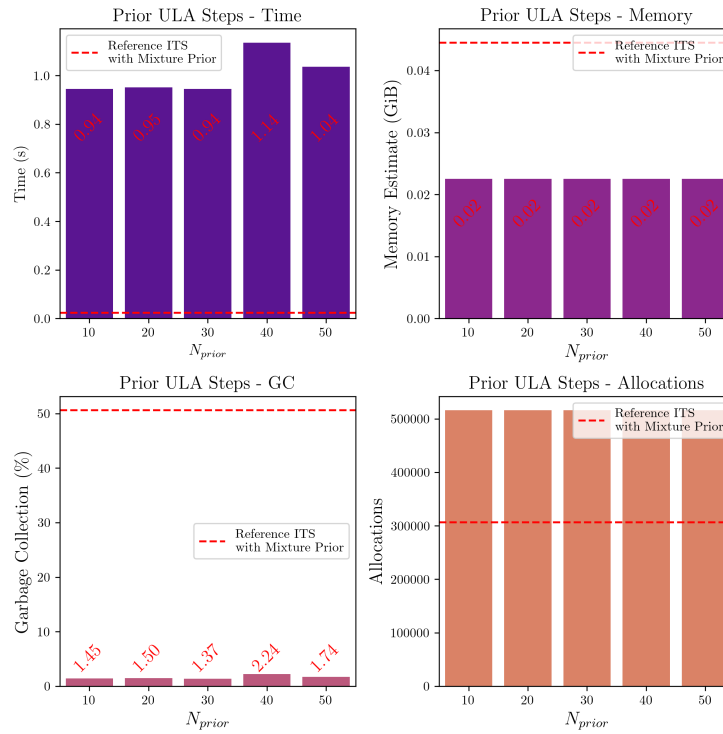


Figure 9: Benchmarks for varying amounts of ULA iterations, N_{prior} , to sample from a deep EBM prior (Tab. 8). Posterior expectations were estimated with an Monte Carlo estimator of the MLE criterion, Eq. 16. All other hyperparameters were kept consistent with Tab. 6. They reflect the computational cost of generating samples from the prior with Eq. 33. The benchmarks for ULA appear relatively constant across different step counts due to Julia’s loop optimizations and efficient memory management. Nevertheless, the reference ITS sampler remains significantly faster in practice. Note: Since the reference ITS sampling executed very rapidly, its relatively high proportion of time attributed to garbage collection is not unexpected.

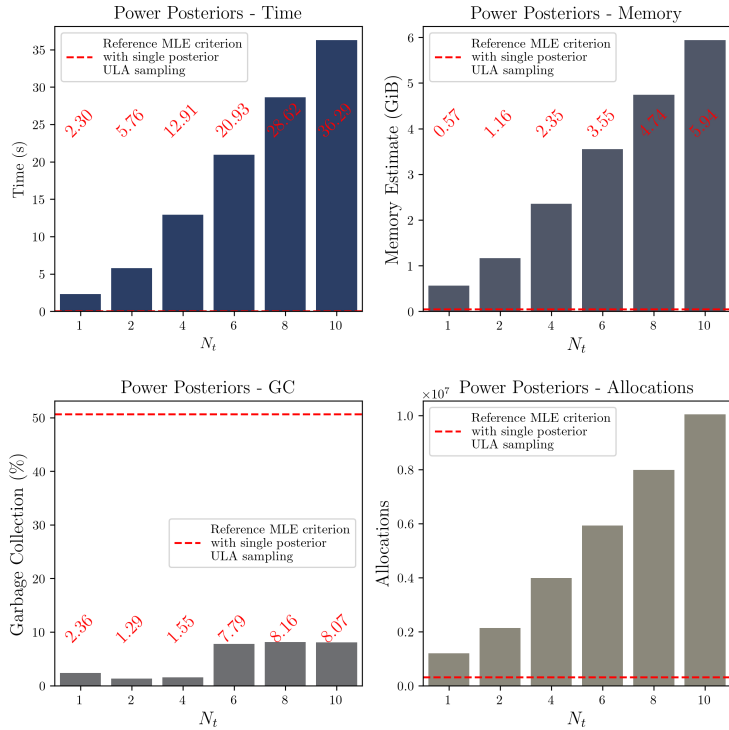


Figure 10: Benchmarks for varying amounts of temperatures, N_t , while using a mixture of EBM priors (Tab. 7) with ITS sampling. Posterior expectations were estimated with SE and population-based ULA. All other hyperparameters were kept consistent with Tab. 6. They reflect the computational cost of performing a single reverse autodifferentiation of the SE criterion, Eq. 31. Note: Since the reference MLE criterion is executed very rapidly, its relatively high proportion of time attributed to garbage collection is not unexpected.

A.3 GUIDANCE ON TEMPERING

A.3.1 CYCLIC ANNEALING

Calderhead & Girolami (2009) demonstrated that uniformly scheduling the discretized temperatures in Eq. 30 results in unequal contributions of adjacent power posteriors to the Thermodynamic Integral. The success of TI and SE, relies on selecting each t_k to ensure sufficient overlap of adjacent power posteriors. This overlap ensures similarity between adjacent power posteriors, as introduced in Sec. A.6.1, which influences the Monte Carlo estimator in Eq. 32, given that SE is an application of importance sampling, (Annis et al., 2019).

This overlap is quantified by the KL divergence term in Eq. 52. Maintaining small KL divergences between adjacent power posteriors can be achieved by clustering temperatures in regions where $P(z | \mathbf{x}^{(b)}, \mathbf{f}, \Phi, t_k)$ changes rapidly. To accomplish this, we follow Calderhead & Girolami (2009) in adopting a power-law relationship to schedule the temperatures of Eq. 30:

$$t_k = \left(\frac{k}{N_t} \right)^p, \quad k = 0, 1, \dots, N_t, \quad (36)$$

The effect of varying p on the schedule between 0 and 1 is visualized in Fig. 11. When $p > 1$, spacing becomes denser near $t = 0$, while $p < 1$ creates denser spacing near $t = 1$. The impact of varying p on the discretized Thermodynamic Integral of Eq. 52 is illustrated in Fig. 12. The plots demonstrate that for $p > 1$, the trapezoidal bins are clustered closer to $t = 0$, concentrating the discrete approximation error towards $t = 1$.

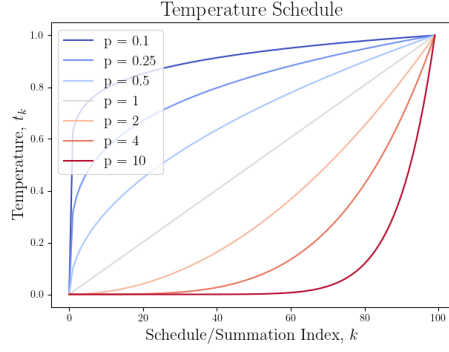


Figure 11: Power-law schedule.

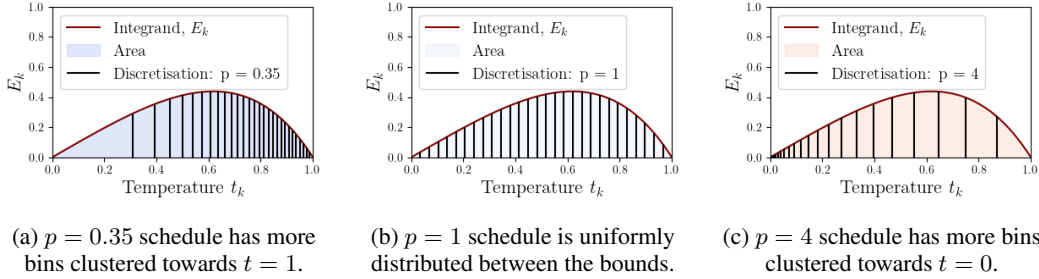


Figure 12: Effect of power-law schedule clusters on integral approximation error. Evaluation points can be skewed towards a particular bound by choosing p . Increasing p provides more tempering, concentrating more evaluation points on smoother likelihoods. Tempering helps to mitigate practical challenges associated with the non-smoothness of the univariate functions in Eq. 1.

The study by Calderhead & Girolami (2009) derives an analytic term for an optimal tempering distribution in the context of linear regression models, where the power posterior in Eq. 29 is used to evaluate the plausibility of model parameters in relation to the data, rather than reflecting a latent variable posterior. However, their findings may not hold in the context of T-KAM and generative modeling, making p and the temperature schedule difficult variables to tune.

Instead, we schedule p cyclically across all parameter updates of T-KAM’s training procedure, similar to the previous work of Fu et al. (2019). The initial and final p ’s and the number of cycles are treated as tunable hyperparameters:

$$\begin{aligned} \delta &= \text{linspace}(0, 2\pi(N_{\text{cycles}} + 0.5); \text{len} = N_{\text{updates}}) \\ p(i) &= p_{\text{init}} + \frac{p_{\text{end}} - p_{\text{init}}}{2} (1 - \cos \delta) \end{aligned} \quad (37)$$

where N_{updates} denotes the total number of parameter updates, i indexes the current training iteration, N_{cycles} is the number of cycles, and δ is a vector of length N_{updates} .

Initializing $p > 1$ focuses learning on smoother likelihoods during the early stages of the cycle, where global features emerge between adjacent power posteriors. As training progresses, T-KAM will have learned the global features sufficiently well, reducing the change of measure between adjacent power posteriors of a $p > 1$ schedule. At this stage, $p(i)$ will have transitioned to $p \leq 1$, thereby shifting T-KAM’s focus towards capturing more detailed features of the posterior landscape, where training is expected to enhance its ability to generate finer details.

Guidance on selecting optimal values for the tempering hyperparameters is provided in Tab. 3.

A.3.2 CHOOSING HYPERPARAMETERS

Table 3: Tempering hyperparameters.

Hyperparameter	Description
$N_t > 1$	Specifies the number of power posteriors, enabling a smooth transition between the prior and posterior. Increasing this improves exploration but also increases cost due to the need for more MALA iterations. Typically, this is limited and therefore guided by hardware availability, such as $N_t = 5$.
$N_{\text{local}} > 1$	Determines the number of ULA or autoMALA iterations per power posterior. Although increasing this value improves the quality of samples at each stage, it also raises the computational cost, much like N_t . It can be kept at a moderate value, such as $N_{\text{local}} = 20$, (based on the recommendations of Nijkamp et al. (2019b;a) regarding short-run Markov chain Monte Carlo).
$N_{\text{unadjusted}} > 1$	Controls the number of autoMALA iterations performed without MH adjustments, reflecting the level of exploration at each power posterior. This can be set to 1, as guided by Biron-Lattes et al. (2024).
$p_{\text{init}} > 1, p_{\text{end}} \leq 1, N_{\text{cycles}}$	Controls the evolution of tempering during training. If the data is expected to have smooth relationships, reduce both p_{init} and p_{end} . For data with finer details, increase both values to allow for better focus on capturing intricate features. Recommended values are $p_{\text{init}} = 4$, and $p_{\text{end}} = 1$, since our experience suggests that power posteriors change rapidly closer to the prior.

A.4 DERIVATIONS AND OTHER IDENTITIES

A.4.1 USEFUL PROOF

The following short proof for a learning gradient with respect to an arbitrary set of parameters, θ , proves useful for other derivations in this study:

$$\begin{aligned} \mathbb{E}_{P(\mathbf{x}|\theta)} [\nabla_{\theta} \log P(\mathbf{x} | \theta)] &= \mathbb{E}_{P(\mathbf{x}|\theta)} \left[\frac{\nabla_{\theta} P(\mathbf{x} | \theta)}{P(\mathbf{x} | \theta)} \right] = \int_{\mathcal{X}} \frac{\nabla_{\theta} P(\mathbf{x} | \theta)}{P(\mathbf{x} | \theta)} dP(\mathbf{x} | \theta) \\ &= \int_{\mathcal{X}} \nabla_{\theta} P(\mathbf{x} | \theta) d\mathbf{x} = \nabla_{\theta} \int_{\mathcal{X}} P(\mathbf{x} | \theta) d\mathbf{x} = \nabla_{\theta} 1 = 0. \end{aligned} \quad (38)$$

A.4.2 MARGINAL LIKELIHOOD

$$\begin{aligned} \log \left(P(\mathbf{x}^{(b)} | \mathbf{f}, \Phi) \right) &= \mathbb{E}_{P(\mathbf{z}|\mathbf{x}^{(b)}, \mathbf{f}, \Phi)} \left[\log \left(P(\mathbf{x}^{(b)}, \mathbf{z} | \mathbf{f}, \Phi) \right) \right] \\ &= \mathbb{E}_{P(\mathbf{z}|\mathbf{x}^{(b)}, \mathbf{f}, \Phi)} \left[\log \left(P(\mathbf{z} | \mathbf{f}) \cdot P(\mathbf{x}^{(b)} | \mathbf{z}, \Phi) \right) \right] \\ &= \mathbb{E}_{P(\mathbf{z}|\mathbf{x}^{(b)}, \mathbf{f}, \Phi)} \left[\log (P(\mathbf{z} | \mathbf{f})) + \log \left(P(\mathbf{x}^{(b)} | \mathbf{z}, \Phi) \right) \right]. \end{aligned} \quad (39)$$

A.4.3 MAXIMUM LIKELIHOOD LEARNING GRADIENT

This proof demonstrates that the learning gradient with respect to an arbitrary set of parameters, θ , is independent of sampling:

$$\begin{aligned} \mathbb{E}_{P(\mathbf{z}|\mathbf{x})} [\nabla_{\theta} \log P(\mathbf{x}, \mathbf{z})] &= \mathbb{E}_{P(\mathbf{z}|\mathbf{x})} [\nabla_{\theta} \log P(\mathbf{z} | \mathbf{x}) + \nabla_{\theta} \log P(\mathbf{x})] \\ &= \mathbb{E}_{P(\mathbf{z}|\mathbf{x})} [\nabla_{\theta} \log P(\mathbf{z} | \mathbf{x})] + \mathbb{E}_{P(\mathbf{z}|\mathbf{x})} [\nabla_{\theta} \log P(\mathbf{x})] \\ &= 0 + \nabla_{\theta} \log P(\mathbf{x}), \end{aligned} \quad (40)$$

where Eq. 38 has been used to zero the expected posterior. This allows gradient flow to be disregarded in sampling procedures as shown in Eq. 16.

A.4.4 CONTRASTIVE DIVERGENCE LEARNING GRADIENT FOR LOG-PRIOR

The learning gradient attributed to the prior can be derived into a contrastive divergence framework, which is more typical of energy-based modeling literature. The prior model is solely dependent on \mathbf{f} in Eq. 4. We can rewrite Eq. 17 as:

$$\nabla_{\mathbf{f}} \log(P(\mathbf{z} | \mathbf{f})) = \nabla_{\mathbf{f}} \sum_{q=1}^{2n_z+1} \sum_{p=1}^{n_z} \log(\pi_{q,p}(z_{q,p})) = \nabla_{\mathbf{f}} \sum_{q=1}^{2n_z+1} \sum_{p=1}^{n_z} f_{q,p}(z_{q,p}) + \log(\pi_0(z_{q,p})) - \log(Z_{q,p}) \quad (41)$$

where $Z_{q,p} = \int_{\mathcal{Z}} \exp(f_{q,p}(z_p)) d\pi_0(z_p)$ is the normalization constant. We can simplify the constant using Eq. 38:

$$\begin{aligned} \mathbb{E}_{P(\mathbf{z}|\mathbf{f})} \left[\nabla_{\mathbf{f}} \log P(\mathbf{z} | \mathbf{f}) \right] &= \mathbb{E}_{P(\mathbf{z}|\mathbf{f})} \left[\nabla_{\mathbf{f}} \sum_{q=1}^{2n_z+1} \sum_{p=1}^{n_z} f_{q,p}(z_{q,p}) + \log(\pi_0(z_{q,p})) - \log(Z_{q,p}) \right] = 0 \\ &= \mathbb{E}_{P(\mathbf{z}|\mathbf{f})} \left[\nabla_{\mathbf{f}} \sum_{q=1}^{2n_z+1} \sum_{p=1}^{n_z} f_{q,p}(z_{q,p}) \right] - \nabla_{\mathbf{f}} \sum_{q=1}^{2n_z+1} \sum_{p=1}^{n_z} \log(Z_{q,p}) = 0 \\ \therefore \nabla_{\mathbf{f}} \sum_{q=1}^{2n_z+1} \sum_{p=1}^{n_z} \log(Z_{q,p}) &= \mathbb{E}_{P(\mathbf{z}|\mathbf{f})} \left[\nabla_{\mathbf{f}} \sum_{q=1}^{2n_z+1} \sum_{p=1}^{n_z} f_{q,p}(z_{q,p}) \right] \end{aligned} \quad (42)$$

Therefore the log-prior gradient of Eq. 41 can be evaluated without quadrature normalization as:

$$\nabla_{\mathbf{f}} \log P(\mathbf{z} | \mathbf{f}) = \nabla_{\mathbf{f}} \sum_{q=1}^{2n_z+1} \sum_{p=1}^{n_z} f_{q,p}(z_{q,p}) - \mathbb{E}_{P(\mathbf{z}|\mathbf{f})} \left[\nabla_{\mathbf{f}} \sum_{q=1}^{2n_z+1} \sum_{p=1}^{n_z} f_{q,p}(z_{q,p}) \right], \quad (43)$$

and the learning gradient attributed to the prior is finalized into a contrastive divergence format:

$$\begin{aligned} \mathbb{E}_{P(\mathbf{z}|\mathbf{x}^{(b)}, \mathbf{f}, \Phi)} \left[\nabla_{\mathbf{f}} [\log P(\mathbf{z} | \mathbf{f})] \right] &= \mathbb{E}_{P(\mathbf{z}|\mathbf{x}^{(b)}, \mathbf{f}, \Phi)} \left[\nabla_{\mathbf{f}} \sum_{q=1}^{2n_z+1} \sum_{p=1}^{n_z} f_{q,p}(z_{q,p}) \right] \\ &\quad - \mathbb{E}_{P(\mathbf{z}|\mathbf{f})} \left[\nabla_{\mathbf{f}} \sum_{q=1}^{2n_z+1} \sum_{p=1}^{n_z} f_{q,p}(z_{q,p}) \right]. \end{aligned} \quad (44)$$

A.4.5 DERIVING THE THERMODYNAMIC INTEGRAL

Starting from the power posterior:

$$P(\mathbf{z} | \mathbf{x}^{(b)}, \mathbf{f}, \Phi, t) = \frac{P(\mathbf{x}^{(b)} | \mathbf{z}, \Phi)^t P(\mathbf{z} | \mathbf{f})}{\mathbf{Z}_t} \quad (45)$$

The partition function \mathbf{Z}_t is given by:

$$\mathbf{Z}_t = \mathbb{E}_{P(\mathbf{z}|\mathbf{f})} \left[P(\mathbf{x}^{(b)} | \mathbf{z}, \Phi)^t \right] \quad (46)$$

Now, differentiating the log-partition function with respect to t :

$$\begin{aligned} \frac{\partial}{\partial t} \log(\mathbf{Z}_t) &= \frac{1}{\mathbf{Z}_t} \frac{\partial}{\partial t} \mathbf{Z}_t = \frac{1}{\mathbf{Z}_t} \mathbb{E}_{P(\mathbf{z}|\mathbf{f})} \left[\frac{\partial}{\partial t} P(\mathbf{x}^{(b)} | \mathbf{z}, \Phi)^t \right] \\ &= \frac{1}{\mathbf{Z}_t} \mathbb{E}_{P(\mathbf{z}|\mathbf{f})} \left[\log P(\mathbf{x}^{(b)} | \mathbf{z}, \Phi) \cdot P(\mathbf{x}^{(b)} | \mathbf{z}, \Phi)^t \right] \\ &= \mathbb{E}_{P(\mathbf{z}|\mathbf{x}^{(b)}, \mathbf{f}, \Phi, t)} \left[\log P(\mathbf{x}^{(b)} | \mathbf{z}, \Phi) \right] \end{aligned} \quad (47)$$

Integrating both sides from 0 to 1:

$$\int_0^1 \frac{\partial}{\partial t} \log(\mathbf{Z}_t) dt = \int_0^1 \mathbb{E}_{P(\mathbf{z}|\mathbf{x}^{(b)}, \mathbf{f}, \Phi, t)} \left[\log P(\mathbf{x}^{(b)} | \mathbf{z}, \Phi) \right] dt \quad (48)$$

Using the fundamental theorem of calculus, (Larson & Edwards, 2008):

$$\int_0^1 \frac{\partial}{\partial t} \log(\mathbf{Z}_t) dt = \log(\mathbf{Z}_{t=1}) - \log(\mathbf{Z}_{t=0}) = \int_0^1 \mathbb{E}_{P(\mathbf{z}|\mathbf{x}^{(b)}, \mathbf{f}, \Phi, t)} \left[\log P(\mathbf{x}^{(b)} | \mathbf{z}, \Phi) \right] dt \quad (49)$$

The limits of the integrals can be expressed as:

$$\begin{aligned} \log(\mathbf{Z}_{t=0}) &= \log \left(\mathbb{E}_{P(\mathbf{z}|\mathbf{f})} \left[P(\mathbf{x}^{(b)} | \mathbf{z}, \Phi)^0 \right] \right) = \log(1) = 0 \\ \log(\mathbf{Z}_{t=1}) &= \log \left(\mathbb{E}_{P(\mathbf{z}|\mathbf{x}^{(b)}, \mathbf{f}, \Phi)} \left[\log P(\mathbf{x}^{(b)} | \mathbf{z}, \Phi) \right] \right) = \log P(\mathbf{x}^{(b)} | \mathbf{f}, \Phi) \end{aligned} \quad (50)$$

Therefore, we obtain the log-marginal likelihood expressed as the Thermodynamic Integral:

$$\log(\mathbf{Z}_{t=1}) - \log(\mathbf{Z}_{t=0}) = \log P(\mathbf{x}^{(b)} | \mathbf{f}, \Phi) = \int_0^1 \mathbb{E}_{P(\mathbf{z}|\mathbf{x}^{(b)}, \mathbf{f}, \Phi, t)} \left[\log P(\mathbf{x}^{(b)} | \mathbf{z}, \Phi) \right] dt \quad (51)$$

A.4.6 DISCRETIZING THE THERMODYNAMIC INTEGRAL

Here, t_k denotes the tempering at the k -th index of the schedule, and N_t is the number of temperatures. As derived by Calderhead & Girolami (2009), Eq. 28 then be evaluated using:

$$\log \left(P(\mathbf{x}^{(b)} | \mathbf{f}, \Phi) \right) = \frac{1}{2} \sum_{k=1}^{N_t} \Delta t_k (E_{k-1} + E_k) + \frac{1}{2} \sum_{k=1}^{N_t} D_{\text{KL}}(P_{t_{k-1}} || P_{t_k}) - D_{\text{KL}}(P_{t_k} || P_{t_{k-1}}) \quad (52)$$

Where:

$$\begin{aligned} \Delta t_k &= t_k - t_{k-1}, \quad E_k = \mathbb{E}_{P(\mathbf{z}|\mathbf{x}^{(b)}, \mathbf{f}, \Phi, t_k)} \left[\log \left(P(\mathbf{x}^{(b)} | \mathbf{z}, \Phi) \right) \right], \\ D_{\text{KL}}(P_{t_{k-1}} || P_{t_k}) &= \mathbb{E}_{P(\mathbf{z}|\mathbf{x}^{(b)}, \mathbf{f}, \Phi, t_{k-1})} \left[\log \left(\frac{P(\mathbf{z} | \mathbf{x}^{(b)}, \mathbf{f}, \Phi, t_{k-1})}{P(\mathbf{z} | \mathbf{x}^{(b)}, \mathbf{f}, \Phi, t_k)} \right) \right] \end{aligned} \quad (53)$$

This reflects the trapezium rule for numerical integration, supported by bias correction to provide an estimate of the Riemann integral that is especially robust to error. The learning gradient derived from the discretized Thermodynamic Integral is unchanged from the MLE gradient in Eq. 16, as demonstrated under Sec. A.4.7.

A.4.7 LEARNING GRADIENT FOR DISCRETIZED THERMODYNAMIC INTEGRAL AND POWER POSTERIOR PARTITION FUNCTION

We can derive the learning gradient of the discretized Thermodynamic Integral in Eq. 52 by reducing it down into a sum of normalizing constants. Starting from the definitions attributed to the KL divergence terms:

$$\begin{aligned} D_{\text{KL}}(P_{t_{k-1}} || P_{t_k}) &= \mathbb{E}_{P(\mathbf{z}|\mathbf{x}^{(b)}, \mathbf{f}, \Phi, t_{k-1})} \left[\log P(\mathbf{z} | \mathbf{x}^{(b)}, \mathbf{f}, \Phi, t_{k-1}) - \log P(\mathbf{z} | \mathbf{x}^{(b)}, \mathbf{f}, \Phi, t_k) \right] \\ \text{and } D_{\text{KL}}(P_{t_k} || P_{t_{k-1}}) &= \mathbb{E}_{P(\mathbf{z}|\mathbf{x}^{(b)}, \mathbf{f}, \Phi, t_k)} \left[\log P(\mathbf{z} | \mathbf{x}^{(b)}, \mathbf{f}, \Phi, t_k) - \log P(\mathbf{z} | \mathbf{x}^{(b)}, \mathbf{f}, \Phi, t_{k-1}) \right] \\ &= -\mathbb{E}_{P(\mathbf{z}|\mathbf{x}^{(b)}, \mathbf{f}, \Phi, t_k)} \left[\log P(\mathbf{z} | \mathbf{x}^{(b)}, \mathbf{f}, \Phi, t_{k-1}) - \log P(\mathbf{z} | \mathbf{x}^{(b)}, \mathbf{f}, \Phi, t_k) \right] \end{aligned} \quad (54)$$

We can leverage Eq. 29 to quantify the log-difference in terms of the change in likelihood contribution plus some normalization constant:

$$\log P(\mathbf{z} | \mathbf{x}^{(b)}, \mathbf{f}, \Phi, t_{k-1}) - \log P(\mathbf{z} | \mathbf{x}^{(b)}, \mathbf{f}, \Phi, t_k) = -\Delta t_k \cdot \log P(\mathbf{x}^{(b)} | \mathbf{z}, \Phi) + \log \left(\frac{\mathbf{Z}_{t_k}}{\mathbf{Z}_{t_{k-1}}} \right) \quad (55)$$

The definitions in Eq. 53 can be used to express the KL divergences in terms of the expected likelihoods:

$$\begin{aligned} \therefore D_{\text{KL}}(P_{t_{k-1}} \| P_{t_k}) &= -\Delta t_k \cdot \mathbb{E}_{P(\mathbf{z} | \mathbf{x}^{(b)}, \mathbf{f}, \Phi, t_{k-1})} \left[\log P(\mathbf{x}^{(b)} | \mathbf{z}, \Phi) \right] + \log \left(\frac{\mathbf{Z}_{t_k}}{\mathbf{Z}_{t_{k-1}}} \right) \\ &= -\Delta t_k \cdot E_{k-1} + \log \left(\frac{\mathbf{Z}_{t_k}}{\mathbf{Z}_{t_{k-1}}} \right) \end{aligned} \quad (56)$$

$$\begin{aligned} \text{and } D_{\text{KL}}(P_{t_k} \| P_{t_{k-1}}) &= \Delta t_k \cdot \mathbb{E}_{P(\mathbf{z} | \mathbf{x}^{(b)}, \mathbf{f}, \Phi, t_k)} \left[\log P(\mathbf{x}^{(b)} | \mathbf{z}, \Phi) \right] - \log \left(\frac{\mathbf{Z}_{t_k}}{\mathbf{Z}_{t_{k-1}}} \right) \\ &= \Delta t_k \cdot E_k - \log \left(\frac{\mathbf{Z}_{t_k}}{\mathbf{Z}_{t_{k-1}}} \right) \end{aligned} \quad (57)$$

Substituting back into Eq. 52, we eliminate the expected likelihood terms:

$$\begin{aligned} \frac{1}{2} \sum_{k=1}^{N_t} D_{\text{KL}}(P_{t_{k-1}} \| P_{t_k}) - D_{\text{KL}}(P_{t_k} \| P_{t_{k-1}}) &= -\frac{1}{2} \sum_{k=1}^{N_t} \Delta t_k (E_{k-1} + E_k) - 2 \log \left(\frac{\mathbf{Z}_{t_k}}{\mathbf{Z}_{t_{k-1}}} \right) \\ \therefore \log \left(P(\mathbf{x}^{(b)} | \mathbf{f}, \Phi) \right) &= \frac{1}{2} \sum_{k=1}^{N_t} \Delta t_k (E_{k-1} + E_k) + \frac{1}{2} \sum_{k=1}^{N_t} D_{\text{KL}}(P_{t_{k-1}} \| P_{t_k}) - D_{\text{KL}}(P_{t_k} \| P_{t_{k-1}}) \\ &= \frac{1}{2} \sum_{k=1}^{N_t} \Delta t_k (E_{k-1} + E_k) - \left[\frac{1}{2} \sum_{k=1}^{N_t} \Delta t_k (E_{k-1} + E_k) - 2 \log \left(\frac{\mathbf{Z}_{t_k}}{\mathbf{Z}_{t_{k-1}}} \right) \right] \\ &= \sum_{k=1}^{N_t} \log \left(\frac{\mathbf{Z}_{t_k}}{\mathbf{Z}_{t_{k-1}}} \right) = \sum_{k=1}^{N_t} \log(\mathbf{Z}_{t_k}) - \log(\mathbf{Z}_{t_{k-1}}) \end{aligned} \quad (58)$$

Following a similar method to Sec. A.4.4 we can use Eq. 38 to express the learning gradient attributed to each normalization constant in a simpler manner:

$$\begin{aligned} &\mathbb{E}_{P(\mathbf{z} | \mathbf{x}^{(b)}, \mathbf{f}, \Phi, t_k)} \left[\nabla_{\mathbf{f}, \Phi} \log P(\mathbf{z} | \mathbf{x}^{(b)}, \mathbf{f}, \Phi, t_k) \right] \\ &= \mathbb{E}_{P(\mathbf{z} | \mathbf{x}^{(b)}, \mathbf{f}, \Phi, t_k)} \left[t_k \cdot \nabla_{\Phi} \log P(\mathbf{x}^{(b)} | \mathbf{z}, \Phi) + \nabla_{\mathbf{f}} \log P(\mathbf{z} | \mathbf{f}) \right] - \nabla_{\mathbf{f}, \Phi} \log(\mathbf{Z}_{t_k}) = 0 \\ \therefore \nabla_{\mathbf{f}, \Phi} \log(\mathbf{Z}_{t_k}) &= \mathbb{E}_{P(\mathbf{z} | \mathbf{x}^{(b)}, \mathbf{f}, \Phi, t_k)} \left[t_k \cdot \nabla_{\Phi} \log P(\mathbf{x}^{(b)} | \mathbf{z}, \Phi) + \nabla_{\mathbf{f}} \log P(\mathbf{z} | \mathbf{f}) \right] \end{aligned} \quad (59)$$

Telescoping the sum in Eq. 58, and noting that $k = 1$ corresponds to the power posterior equaling the prior, and $k = N_t$ to the posterior, Eq. 58 yields T-KAM's learning gradient:

$$\begin{aligned} \nabla_{\mathbf{f}, \Phi} \log \left(P(\mathbf{x}^{(b)} | \mathbf{f}, \Phi) \right) &= \sum_{k=1}^{N_t} \nabla_{\mathbf{f}, \Phi} \log(\mathbf{Z}_{t_k}) - \nabla_{\mathbf{f}, \Phi} \log(\mathbf{Z}_{t_{k-1}}) \\ &= \nabla_{\mathbf{f}, \Phi} \log(\mathbf{Z}_{t_{N_t}}) - \nabla_{\mathbf{f}, \Phi} \log(\mathbf{Z}_{t_0}) \\ &= \mathbb{E}_{P(\mathbf{z} | \mathbf{x}^{(b)}, \mathbf{f}, \Phi)} \left[\nabla_{\mathbf{f}} \log P(\mathbf{z} | \mathbf{f}) + \nabla_{\Phi} \log P(\mathbf{x}^{(b)} | \mathbf{z}, \Phi) \right] \\ &\quad - \underbrace{\mathbb{E}_{P(\mathbf{z} | \mathbf{f})} \left[\nabla_{\mathbf{f}} \log P(\mathbf{z} | \mathbf{f}) \right]}_{=0 \text{ (Eq. 38)}}. \end{aligned} \quad (60)$$

A.5 HYPERPARAMETERS AND TRAINING DETAILS

Table 4: Hyperparameters for Sec. 3.1.1.

EBM Prior		
layer_widths	p, q	40, 81
spline_type	(-)	variable
spline_activation	(-)	Silu
layer_norm	(-)	true
quadrature_method	(-)	gausslegendre
spline_degree	d	3
grid_size	N_{grid}	RBF: 20 FFT: 50
grid_update_ratio	α_{grid}	0.05
grid_range	$[z_{\min}, z_{\max}]$	Uniform: $[0, 1]$ Lognormal: $[0, 4]$ Gaussian: $[-1.2, 1.2]$
Spline basis ε init.	ε	0.1
Spline basis μ scaling	μ	1.0
Basis activation scaling	σ_b	1.0
Basis spline scaling	σ_s	1.0
Initial basis param.	τ_0	1.0
Train basis param.	$\tau_{\text{trainable}}$	true
GaussQuad_nodes	N_{quad}	100
Use mixture prior	(-)	false
KAN Likelihood		
hidden_widths	$q, 2q + 1$	81, 162
All other KAN hparams	Identical to EBM Prior	
generator_variance	σ_ε	1.0
output_activation	σ_{act}	sigmoid
Importance sampling resampler	resampler	residual
ESS threshold	γ	0.5
Grid updating		
update_prior_grid	(-)	true
update_llhood_grid	(-)	true
num_grid_updating_samples	(-)	50
grid_update_frequency	(-)	100
grid_update_decay	(-)	0.999
Training		
batch_size	N_x	100
importance_sample_size	N_s	100
Training examples	N_{train}	20,000
Testing examples	N_{test}	100
num_generated_samples	(-)	3,000
Number of epochs	N_{epochs}	10
eps	ϵ	0.001
Optimizer		
type	(-)	adam
learning_rate	η_{LR}	0.001
betas	(-)	(0.9, 0.999)

Table 5: Hyperparameters for Sec. 3.1.2.

EBM Prior		
layer_widths	p, q	40, 81
spline_type	(-)	variable
spline_activation	(-)	Silu
layer_norm	(-)	true
quadrature_method	(-)	gausslegendre
spline_degree	d	3
grid_size	N_{grid}	RBF: 20 FFT: 50
grid_update_ratio	α_{grid}	0.05
grid_range	$[z_{\min}, z_{\max}]$	Uniform: $[0, 1]$ Lognormal: $[0, 4]$ Gaussian: $[-1.2, 1.2]$
Spline basis ε init.	ε	0.1
Spline basis μ scaling	μ	1.0
Basis activation scaling	σ_b	1.0
Basis spline scaling	σ_s	1.0
Initial basis param.	τ_0	1.0
Train basis param.	$\tau_{\text{trainable}}$	true
GaussQuad_nodes	N_{quad}	100
Use mixture prior	(-)	false
KAN Likelihood		
hidden_widths	$q, 2q + 1$	81, 162
All other KAN hparams	Identical to EBM Prior	
generator_variance	σ_ε	0.1
output_activation	σ_{act}	sigmoid
Importance sampling resampler	resampler	residual
ESS threshold	γ	0.5
Grid updating		
update_prior_grid	(-)	true
update_llhood_grid	(-)	true
num_grid_updating_samples	(-)	100
grid_update_frequency	(-)	100
grid_update_decay	(-)	0.999
Training		
batch_size	N_x	50
importance_sample_size	N_s	50
Training examples	N_{train}	1,000
Testing examples	N_{test}	1,000
num_generated_samples	(-)	3,000
Number of epochs	N_{epochs}	600
eps	ϵ	0.001
Optimizer		
type	(-)	adam
learning_rate	η_{LR}	0.001
betas	(-)	(0.9, 0.999)

Table 6: Hyperparameters for Sec. 3.2.

EBM Prior		
layer_widths	p, q	See Sec. A.5.1
spline_type	(-)	Cheby
spline_activation	(-)	Silu
layer_norm	(-)	false
quadrature_method	(-)	gausslegendre
spline_degree	d	3
grid_size	N_{grid}	0, (Chebyshev requires no grid)
grid_update_ratio	α_{grid}	N/A
grid_range	$[z_{\text{min}}, z_{\text{max}}]$	$[-1.2, 1.2]$
Spline basis ε init.	ε	0.1
Spline basis μ scaling	μ	1.0
Basis activation scaling	σ_b	1.0
Basis spline scaling	σ_s	1.0
Initial basis param.	τ_0	1.01
Train basis param.	$\tau_{\text{trainable}}$	false
GaussQuad_nodes	N_{quad}	100
Use mixture prior	(-)	variable
KAN Likelihood		
cnn_widths	(-)	See Sec. A.5.1
All other KAN hparams		N/A
generator_variance	σ_ε	0.3
output_activation	σ_{act}	sigmoid
Importance sampling resampler	resampler	Not used
ESS threshold	γ	N/A
Grid updating		
update_prior_grid	(-)	false
update_llhood_grid	(-)	false
Training		
batch_size	N_x	100
importance_sample_size	N_s	N/A
Training examples	N_{train}	40,000
Testing examples	N_{test}	100
num_generated_samples	(-)	3,000
Number of epochs	N_{epochs}	20
eps	ϵ	0.0001
Optimizer		
type	(-)	adam
learning_rate	η_{LR}	0.0005
betas	(-)	(0.9, 0.999)
PRIOR LANGEVIN		
iters	N_{local}	60
step_size	η	0.16
POSTERIOR LANGEVIN		
iters	N_{local}	SVHN: 20 CIFAR10: 40
step_size	η	0.01
THERMODYNAMIC INTEGRATION		
iters	N_{local}	20
num_temps	N_t	5
Initial exponent in power law schedule	p_{start}	4
Final exponent in power law schedule	p_{end}	1
num_cycles	N_{cycles}	0
Global swap frequency, replica_exchange_frequency	(-)	1

A.5.1 SVHN & CIFAR-10 ARCHITECTURES

Table 7: Dense Chebyshev KAN architecture for mixture prior model

Layer	Operation	Output Dim.
Input	Latent vector z	$p = 100$
100	Dense(100)	$q = 201$

sizes=[100,201]

Table 8: Dense Chebyshev KAN architecture for deep prior model

Layer	Operation	Output Dim.
Input	Latent vector z	$p = 100$
100	Dense(100)	200
200	Dense(200)	200
200	Dense(200)	$q = 1$

sizes=[100,200,200,1]

Table 9: CNN Generator Architecture for SVHN

Layer	Operation	Output Shape	Stride
Input	Latent vector z reshaped	$1 \times 1 \times q$	–
1	4×4 convT(512), LeakyReLU	$4 \times 4 \times 512$	1
2	4×4 convT(256), LeakyReLU	$8 \times 8 \times 256$	2
3	4×4 convT(128), LeakyReLU	$16 \times 16 \times 128$	2
4	4×4 convT(3), Sigmoid	$32 \times 32 \times 3$	2

Config: kernel=4, strides=1/2/2/2, paddings=0/1/1/1, activation=LeakyReLU, batchnorm=False

Table 10: CNN Generator Architecture for CIFAR-10

Layer	Operation	Output Shape	Stride
Input	Latent vector z reshaped	$1 \times 1 \times q$	–
1	8×8 convT(1024), LeakyReLU	$8 \times 8 \times 1024$	1
2	4×4 convT(512), LeakyReLU	$16 \times 16 \times 512$	2
3	4×4 convT(256), LeakyReLU	$32 \times 32 \times 256$	2
4	3×3 convT(3), Sigmoid	$32 \times 32 \times 3$	1

Config: kernel=8/4/4/3, strides=1/2/2/1, paddings=0/1/1/1, activation=LeakyReLU, batchnorm=False

A.6 SAMPLING THEORY

This section provides more detail regarding T-KAM’s sampling procedures.

A.6.1 IMPORTANCE SAMPLING

Importance Sampling (IS) is a Monte Carlo method rooted in the measure-theoretic formulation of probability. It enables the estimation of expectations with respect to one probability measure using samples drawn from another. For a detailed exposition, see Kloek & van Dijk (1978).

The Radon-Nikodym derivative

IS involves rewriting the expectation of an arbitrary function, $\rho(\mathbf{z})$, under the target measure, $P(\mathbf{z})$, in terms of a more tractable proposal measure, $Q(\mathbf{z})$. Specifically, we use the Radon-Nikodym derivative $\frac{dP}{dQ}$ to rewrite the expectation of an arbitrary function of \mathbf{z} , denoted as $\rho(\mathbf{z})$:

$$\mathbb{E}_{P(\mathbf{z})}[\rho(\mathbf{z})] = \int_{\bar{\mathcal{Z}}} \rho(\mathbf{z}) dP(\mathbf{z}) = \int_{\bar{\mathcal{Z}}} \rho(\mathbf{z}) \cdot \frac{dP}{dQ} dQ(\mathbf{z}). \quad (61)$$

Here, $\frac{dP}{dQ}$ acts as a weight that adjusts the contribution of each sample to account for the difference between the target and proposal measures. This requires that the proposal measure Q is absolutely continuous with respect to the target measure P , i.e. $Q(A) = 0$ implies $P(A) = 0$, for every measurable subset $A \in \mathcal{Z}$.

In the context of T-KAM, the target distribution is the posterior, $P(\mathbf{z} \mid \mathbf{x}^{(b)}, \mathbf{f}, \Phi)$, which is proportional to the product of the likelihood and the prior:

$$P(\mathbf{z} \mid \mathbf{x}^{(b)}, \mathbf{f}, \Phi) \propto P(\mathbf{x}^{(b)} \mid \mathbf{z}, \Phi) \cdot P(\mathbf{z} \mid \mathbf{f}). \quad (62)$$

The exact normalization constant, (the marginal likelihood $P(\mathbf{x}^{(b)} \mid \mathbf{f}, \Phi)$), is intractable, but Importance Sampling circumvents the need to compute it explicitly. Instead, the expectation of $\rho(\mathbf{z})$ under the posterior can be expressed as:

$$\mathbb{E}_{P(\mathbf{z} \mid \mathbf{x}^{(b)}, \mathbf{f}, \Phi)}[\rho(\mathbf{z})] = \int_{\bar{\mathcal{Z}}} \rho(\mathbf{z}) w(\mathbf{z}) dQ(\mathbf{z}), \quad (63)$$

where the importance weights $w(\mathbf{z})$ are given by:

$$w(\mathbf{z}) = \frac{P(\mathbf{z} \mid \mathbf{x}^{(b)}, \mathbf{f}, \Phi)}{Q(\mathbf{z})} = \frac{P(\mathbf{x}^{(b)} \mid \mathbf{z}, \Phi) \cdot P(\mathbf{z} \mid \mathbf{f})}{Q(\mathbf{z})}. \quad (64)$$

Proposal distribution and importance weights

A practical choice for the proposal distribution $Q(\mathbf{z})$ is the prior, $P(\mathbf{z} \mid \mathbf{f})$, given the availability of draws from the prior using the method outlined in Sec. 2.4.3. This simplifies the importance weights, as the prior has a tractable form and covers the support of the posterior. This yields:

$$w(\mathbf{z}^{(s)}) = P(\mathbf{x}^{(b)} \mid \mathbf{z}^{(s)}, \Phi) \propto \exp(\log(P(\mathbf{x}^{(b)} \mid \mathbf{z}^{(s)}, \Phi))). \quad (65)$$

This reflects that the likelihood now directly informs how much weight to assign to each sample \mathbf{z} . Intuitively, samples that better explain the observed data $\mathbf{x}^{(b)}$, (as measured by the likelihood), are given higher importance. Using the definition of softmax, the normalized weights are given by:

$$\frac{w(\mathbf{z}^{(s)})}{\sum_{r=1}^{N_s} w(\mathbf{z}^{(r)})} = \text{softmax}_s \left(\log(P(\mathbf{x}^{(b)} \mid \mathbf{z}^{(s)}, \Phi)) \right). \quad (66)$$

Resampling

The suitability of these weights depends on how well $Q(\mathbf{z})$ matches the posterior. In T-KAM, there is likely to be significant mismatch due to the complexity of the likelihood models described in Eq. 20. Consequently, the weights will exhibit high variance, resulting in many samples contributing minimally. This reduces the Effective Sample Size (ESS) and introduces bias into the estimates.

To address this, the weights are resampled before proceeding with the posterior expectation. This is accomplished by using one of the methods outlined by Douc et al. (2005), whenever the ESS falls below a certain threshold determined by Eq. 26. Resampling redistributes the sample weights, creating a new population with uniformly distributed weights while preserving the statistical properties of the original distribution. As training progresses and the prior becomes a better match for the posterior, the need for resampling decreases.

Importance Sampling estimator

To estimate the expectation, we draw N_s independent samples $\{\mathbf{z}^{(s)}\}_{s=1}^{N_s} \sim Q(\mathbf{z})$ using the procedure outlined in Sec. 2.4.3 and compute a weighted sum:

$$\mathbb{E}_{P(\mathbf{z} \mid \mathbf{x}^{(b)}, \mathbf{f}, \Phi)}[\rho(\mathbf{z})] \approx \sum_{s=1}^{N_s} \rho(\mathbf{z}_{\text{resampled}}^{(s)}) \cdot w_{\text{norm, resampled}}(\bar{\mathbf{z}}_{\text{resampled}}^{(s)}). \quad (67)$$

The estimator is unbiased, implying that its expectation matches the true posterior expectation. As $N_s \rightarrow \infty$, the approximation converges almost surely to the true value, provided that $Q(\mathbf{z})$ sufficiently covers the posterior to ensure a well-conditioned Radon-Nikodym derivative. This estimator is used for the log-marginal likelihood and its gradient in Eqs. 15 & 16, since it provides a means of estimating expectations with respect to the posterior distribution.

A.6.2 RESIDUAL RESAMPLING

In this study, we adopted residual resampling to redraw weights. This redistributes the population of latent samples according to the normalized weights of Sec. A.6.1. The procedure is only conducted when Eq. 26 regarding ESS is satisfied:

1. **Integer replication:** The sample, s , is replicated r_s times, where:

$$r_s = \left\lfloor N_s \cdot w_{\text{norm}}(\mathbf{z}^{(s)}) \right\rfloor \quad (68)$$

2. **Residual weights:** The total number of replicated samples after the previous stage will be $\sum_{s=1}^{N_s} r_s$. Therefore, $N_s - \sum_{s=1}^{N_s} r_s$ remain, which must be resampled using the residuals:

$$w_{\text{residual}}(\mathbf{z}^{(s)}) = w_{\text{norm}}(\mathbf{z}^{(s)}) \cdot (N_s - r_s)$$

$$w_{\text{norm, residual}}(\mathbf{z}^{(s)}) = \frac{w_{\text{residual}}(\mathbf{z}^{(s)})}{\sum_{s=1}^{N_s} w_{\text{residual}}(\mathbf{z}^{(s)})} \quad (69)$$

If a sample has been replicated at the previous stage, then its corresponding $w_{\text{norm, residual}}$ will be reduced, leading to a lower probability of it being resampled again.

3. **Resample:** The remaining samples are drawn with multinomial resampling, based on the cumulative distribution function of the residuals:

$$k^* = \min \left\{ j \mid \sum_{s=1}^j w_{\text{norm, residual}}(\mathbf{z}^{(s)}) \geq u_j \right\} \quad \text{where } u_j \sim \mathcal{U}([0, 1]). \quad (70)$$

where k^* represents the index of the sample to keep.

A.6.3 METROPOLIS-ADJUSTED LANGEVIN ALGORITHM (MALA)

The Metropolis-Adjusted Langevin Algorithm (MALA) (Rosky et al., 1978a; Zhu & Mumford, 1998), is a Markov Chain Monte Carlo (MCMC) method designed to sample from complex distributions by leveraging gradient information. It constructs a proposal mechanism that efficiently explores the target measure by combining stochastic perturbations with information from the target's local geometry to propose local moves, thereby refining the standard Metropolis-Hastings (MH) algorithm (Hastings, 1970).

MALA operates on the target (power) posterior $P(\mathbf{z} \mid \mathbf{x}^{(b)}, \mathbf{f}, \Phi, t_k)$. The algorithm constructs a sequence of random variables $\{\mathbf{z}^{(i, t_k)}\}_{i=1}^{\infty}$ that forms a Markov chain converging in distribution to the target measure. The target posterior measure, $P(\mathbf{z} \mid \mathbf{x}^{(b)}, \mathbf{f}, \Phi, t_k)$, is:

$$\log P(\mathbf{z} \mid \mathbf{x}^{(b)}, \mathbf{f}, \Phi, t_k) = \log P(\mathbf{x}^{(b)} \mid \mathbf{z}, \Phi)^{t_k} + \log P(\mathbf{z} \mid \mathbf{f}) - \text{const}, \quad (71)$$

MALA

Starting with the initial state of the first chain, $\mathbf{z}^{(1, t_1)} \sim Q(\mathbf{z}) = P(\mathbf{z} \mid \mathbf{f})$, the local state within a temperature is updated as follows:

1. **Langevin diffusion:** A new state $\mathbf{z}'^{(i, t_k)}$ is proposed for a local chain, operating with a specific t_k , using a transition kernel inspired by (overdamped) Langevin dynamics (Roberts

& Stramer, 2002; Brooks et al., 2011):

$$\textbf{Target: } \log \gamma \left(\mathbf{z}'^{(i, t_k)} \right) \propto \log P(\mathbf{x}^{(b)} \mid \mathbf{z}, \Phi)^{t_k} + \log P(\mathbf{z} \mid \mathbf{f})$$

$$\textbf{Proposal: } \mathbf{z}'^{(i, t_k)} \mid \mathbf{z}^{(i, t_k)} \sim q \left(\mathbf{z}'^{(i, t_k)} \mid \mathbf{z}^{(i, t_k)} \right)$$

$$\textbf{Kernel: } q(\mathbf{z}'^{(i, t_k)} \mid \mathbf{z}^{(i, t_k)}) = \mathcal{N} \left(\mathbf{z}'^{(i, t_k)}; \mathbf{z}^{(i, t_k)} + \frac{\eta}{2} \mathbf{C} \cdot \nabla_{\mathbf{z}} \log \gamma \left(\mathbf{z}'^{(i, t_k)} \right), \left(\sqrt{\eta} \cdot \mathbf{C}^{\frac{1}{2}} \right)^2 \right), \quad (72)$$

where $\eta > 0$ is the step size, $\nabla_{\mathbf{z}} \log \gamma$ is the log-posterior gradient with respect to $\mathbf{z}^{(i, t_k)}$, and \mathbf{C} is a pre-conditioning, positive-definite matrix, (for example, the identity matrix, \mathbf{I}).

2. **MH criterion:** Once $N_{\text{unadjusted}}$ iterations have elapsed, Metropolis-Hastings adjustments, (MH) (Metropolis & Ulam, 1949), are introduced. The criterion for the local proposal is:

$$r_{\text{local}} = \frac{\gamma \left(\mathbf{z}'^{(i, t_k)} \right) q \left(\mathbf{z}^{(i, t_k)} \mid \mathbf{z}'^{(i, t_k)} \right)}{\gamma \left(\mathbf{z}^{(i, t_k)} \right) q \left(\mathbf{z}'^{(i, t_k)} \mid \mathbf{z}^{(i, t_k)} \right)}, \quad (73)$$

3. **Acceptance:** The proposal is accepted with probability $\min(1, r_{\text{local}})$. If accepted, $\mathbf{z}^{(i+1, t_k)} = \mathbf{z}'^{(i, t_k)}$; otherwise, the current state is retained: $\mathbf{z}^{(i+1, t_k)} = \mathbf{z}^{(i, t_k)}$.
4. **Global Swaps:** Global swaps are proposed and accepted subject to the criterion outlined in Eq. 34

Convergence

Under mild regularity conditions, the local Markov chain $\{\mathbf{z}^{(i, t_k)}\}$ generated by MALA converges in distribution to $P(\mathbf{z} \mid \mathbf{x}^{(b)}, \mathbf{f}, \Phi, t_k)$ as $N_{\text{local}} \rightarrow \infty$. The proposal mechanism in Eq. 72 ensures that the chain mixes efficiently, particularly in high-dimensional spaces, provided that the step size η is tuned appropriately. The algorithm provides theoretical guarantees of the target, due to its satisfaction of detailed balance under Eq. 73:

$$\gamma \left(\mathbf{z}^{(i, t_k)} \right) q \left(\mathbf{z}'^{(i, t_k)} \mid \mathbf{z}^{(i, t_k)} \right) = \gamma \left(\mathbf{z}'^{(i, t_k)} \right) q \left(\mathbf{z}^{(i, t_k)} \mid \mathbf{z}'^{(i, t_k)} \right), \quad (74)$$

ensuring that the stationary distribution of the local chain matches the local target.

A.6.4 AUTOMALA

More details on the Metropolis-adjusted Langevin Algorithm (MALA) are provided in Sec. A.6.3.

Selecting an appropriate step size for unaltered MALA presents a challenge, particularly for SE, as each power posterior exhibits distinct local curvature. To address this, we adaptively tune the step size with autoMALA (Biron-Lattes et al., 2024), which reinterprets MALA as Hamiltonian Monte Carlo (HMC) with a single leapfrog step (Duane et al., 1987).

The algorithm operates locally on a target power posterior $P(\mathbf{z} \mid \mathbf{x}^{(b)}, \mathbf{f}, \Phi, t_k)$. It constructs a sequence of random variables per temperature, $\{\mathbf{z}^{(i, t_k)}\}_{i=1}^{\infty}$, that forms a Markov chain converging in distribution to the local target:

$$\log \gamma \left(\mathbf{z}'^{(i, t_k)} \right) = \log P(\mathbf{z}^{(i, t_k)} \mid \mathbf{x}^{(b)}, \mathbf{f}, \Phi, t_k) \propto \log P(\mathbf{x}^{(b)} \mid \mathbf{z}^{(i, t_k)}, \Phi)^{t_k} + \log P(\mathbf{z}^{(i, t_k)} \mid \mathbf{f}).$$

Starting with the initial state of the first chain, $\mathbf{z}^{(1, t_1)} \sim Q(\mathbf{z}) = P(\mathbf{z} \mid \mathbf{f})$, the local state within a temperature is updated as follows:

1. **Acceptance thresholds:** Two bounding acceptance thresholds are sampled uniformly:

$$a, b \sim \mathcal{U} \left((a, b); \mathbf{0}, \mathbf{1} \right), \quad (a, b) \in [0, 1]^2, \quad b > a \quad (75)$$

2. **Mass matrix:** Random pre-conditioning matrices are initialized per latent dimension:

$$\varepsilon^{(i, t_k)} \sim \text{Beta}_{01} \left(1, 1; \left[\frac{1}{2}, \frac{2}{3} \right] \right),$$

$$M_{p,p}^{1/2 (i, t_k, q)} = \varepsilon^{(i, t_k)} \cdot \Sigma_{p,p}^{-1/2 (i, t_k, q)} + (1 - \varepsilon^{(i, t_k)}), \quad (76)$$

where $\Sigma_{p,p}^{(i, t_k, q)} = \text{VAR}_s \left[\tilde{z}_{q,p}^{(i, t_k, s)} \right]$. Here, $\text{Beta}_{01} [a, b; c, d]$ denotes a zero-one-inflated Beta distribution. The parameters $a, b > 0$ represent the shape parameters of the Beta distribution, while $c, d \in [0, 1]^2$ specify the probabilities governing the mixture. The positive definite mass matrix, \mathbf{M} , can be related to Eq. 72 as $\mathbf{M} = \mathbf{C}^{-1}$, and is efficient to invert as a diagonal matrix.

3. **Leapfrog proposal:** The following transition is proposed for a local chain, t_k , with an adaptive step size, $\eta^{(i, t_k)}$:

$$\mathbf{p}^{(i, t_k)} \sim \mathcal{N} \left(\mathbf{p}; \mathbf{0}, \mathbf{M}^{(i, t_k)} \right)$$

$$\mathbf{p}'_{1/2 (i, t_k)} = \mathbf{p}^{(i, t_k)} + \frac{\eta^{(i, t_k)}}{2} \nabla_{\mathbf{z}} \log \gamma \left(\mathbf{z}'^{(i, t_k)} \right)$$

$$\mathbf{z}'^{(i, t_k)} = \mathbf{z}^{(i, t_k)} + \eta^{(i, t_k)} \left(\mathbf{M}^{-1} \mathbf{p}'_{1/2} \right)^{(i, t_k)}$$

$$\hat{\mathbf{p}}^{(i, t_k)} = \mathbf{p}'_{1/2} + \frac{\eta^{(i, t_k)}}{2} \nabla_{\mathbf{z}} \log \gamma \left(\mathbf{z}'^{(i, t_k)} \right)$$

$$\mathbf{p}'^{(i, t_k)} = -\hat{\mathbf{p}}^{(i, t_k)}, \quad (77)$$

4. **MH criterion:** Once $N_{\text{unadjusted}}$ iterations have elapsed, Metropolis-Hastings (MH) adjustments are introduced. The MH acceptance criterion for the local proposal is:

$$r_{\text{local}} = \frac{\gamma \left(\mathbf{z}'^{(i, t_k)} \right) \mathcal{N} \left(\mathbf{p}'^{(i, t_k)}; \mathbf{0}, \mathbf{M}^{(i, t_k)} \right)}{\gamma \left(\mathbf{z}^{(i, t_k)} \right) \mathcal{N} \left(\mathbf{p}^{(i, t_k)}; \mathbf{0}, \mathbf{M}^{(i, t_k)} \right)}, \quad (78)$$

5. **Step size adaptation:** Starting with an initial estimate, $\eta_{\text{init}}^{(i, t_k)}$, set as the average accepted step size from the previous training iteration, (used as a simple alternative to the round-based tuning algorithm proposed by Biron-Lattes et al. (2024)), the step size is adjusted as follows:

- If $a < r_{\text{local}} < b$, then $\eta^{(i, t_k)} = \eta_{\text{init}}^{(i, t_k)}$
- If $r_{\text{local}} \leq a$, then $\eta'^{(i, t_k)} = \eta_{\text{init}}^{(i, t_k)} / \Delta \eta^k$, where $k \leftarrow k + 1$ is chosen recursively until $r_{\text{local}} > a$, and the step size is accepted, $\eta^{(i, t_k)} = \eta'^{(i, t_k)}$
- If $r_{\text{local}} \geq b$, then $\eta'^{(i, t_k)} = \eta_{\text{init}}^{(i, t_k)} \cdot \Delta \eta^k$, where $k \leftarrow k + 1$ is chosen recursively until $r_{\text{local}} < b$, and the step size is accepted, $\eta^{(i, t_k)} = \eta'^{(i, t_k)} / \Delta \eta$

Here, $\Delta \eta$ is a tunable hyperparameter that controls the rate of step size adaptation. To improve efficiency in our implementation, tuning is prematurely terminated when $\eta^{(i, t_k)}$ falls out of a user-defined range, $[\eta_{\text{min}}, \eta_{\text{max}}]$. Excessively large or small step sizes are not beneficial, so preventing the algorithm from searching extreme values saves time without compromising performance.

6. **Reversibility check:** If the step size was modified, the reversibility of the update in Eq. 77 is verified before proceeding with MH acceptance. If $\eta_{\text{init}}^{(i, t_k)}$ cannot be recovered from the reversed step-size adjustment process with the proposed state, $\{ \mathbf{z}'^{(i, t_k)}, \mathbf{p}'^{(i, t_k)}, \eta^{(i, t_k)} \}$, the proposal is rejected regardless of the outcome of the MH adjustment.
7. **Acceptance:** The proposal is accepted with probability $\min(1, r_{\text{local}})$. If accepted, $\mathbf{z}^{(i+1, t_k)} = \mathbf{z}'^{(i, t_k)}$; otherwise, the current state is retained: $\mathbf{z}^{(i+1, t_k)} = \mathbf{z}^{(i, t_k)}$.
8. **Global Swaps:** Global swaps are proposed and accepted subject to Eq. 34

A.7 20×20 IMAGE GRIDS

A.7.1 MNIST

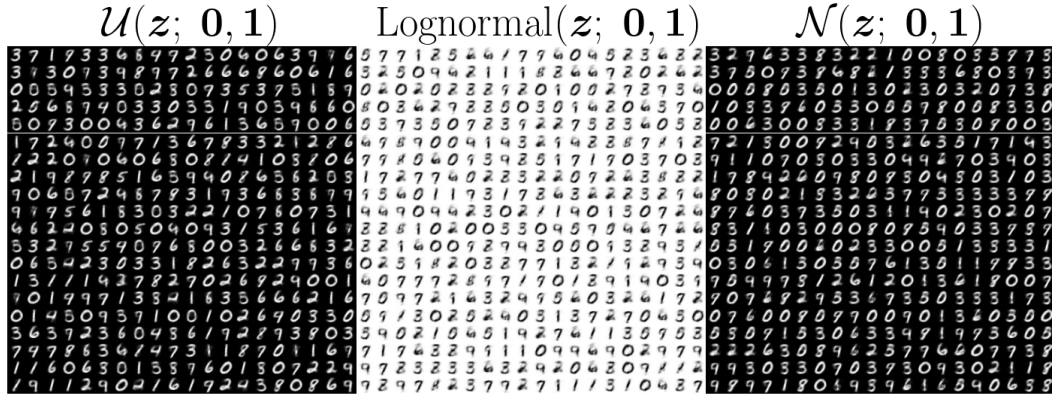


Figure 13: Generated MNIST, (Deng, 2012), after 2,000 parameter updates using MLE / IS adhering to KART’s structure. Uniform, lognormal, and Gaussian priors are contrasted using Radial Basis Functions, (Li, 2024). Lognormal is inverted for clarity.

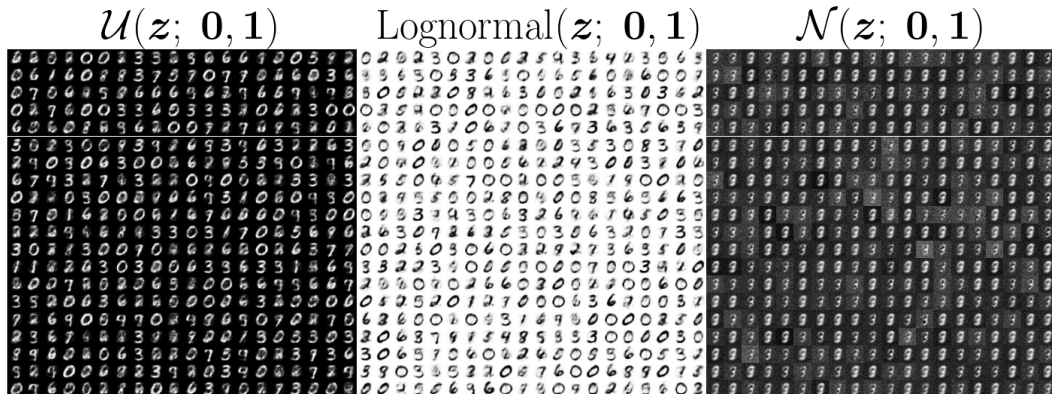


Figure 14: Generated MNIST, (Deng, 2012), after 2,000 parameter updates using MLE / IS adhering to KART’s structure. Uniform, lognormal, and Gaussian priors are contrasted using Fourier Bases, (Xu et al., 2024). Lognormal is inverted for clarity.

A.7.2 FMNIST

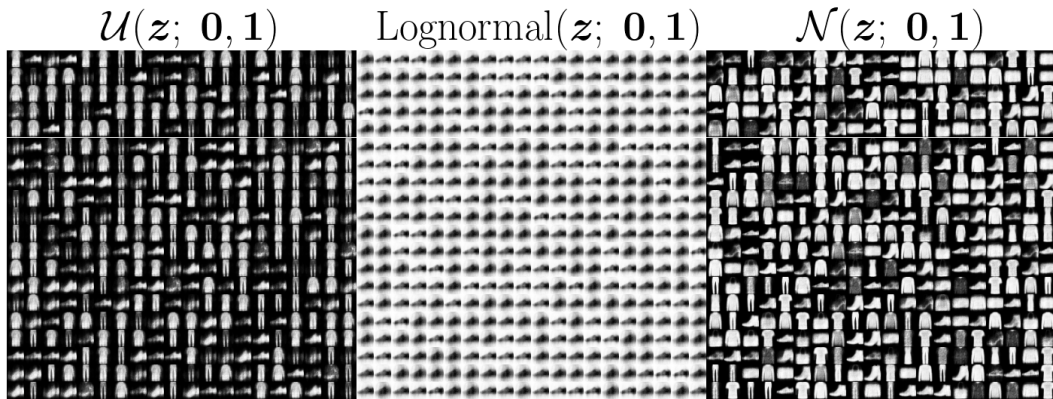


Figure 15: Generated FMNIST, (Xiao et al., 2017), after 2,000 parameter updates using MLE / IS adhering to KART's structure. Uniform, lognormal, and Gaussian priors are contrasted using Radial Basis Functions, (Li, 2024). Lognormal is inverted for clarity.

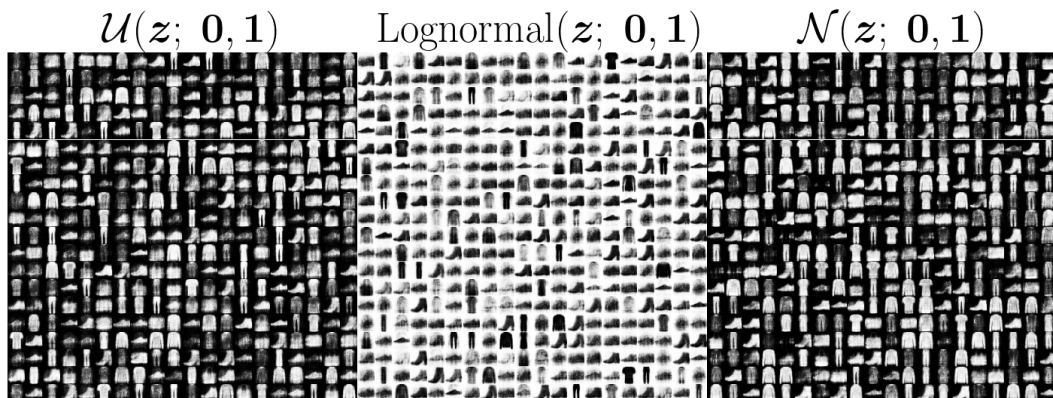


Figure 16: Generated FMNIST, (Xiao et al., 2017), after 2,000 parameter updates using MLE / IS adhering to KART's structure. Uniform, lognormal, and Gaussian priors are contrasted using Fourier Bases, (Xu et al., 2024). Lognormal is inverted for clarity.

A.7.3 DARCY FLOW

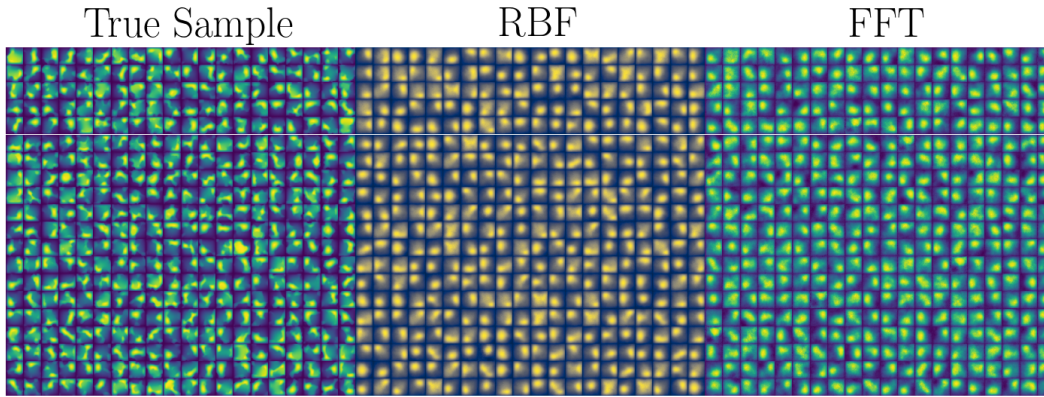


Figure 17: Generated 2D Darcy flow pressures, (Li et al., 2021), after 12,000 parameter updates using MLE / IS while adhering to KART. Radial Basis Functions, (RBFs) (Li, 2024), are contrasted against Fourier bases, (FFTs) (Xu et al., 2024), using Gaussian latent priors. RBF is colored differently for clarity.

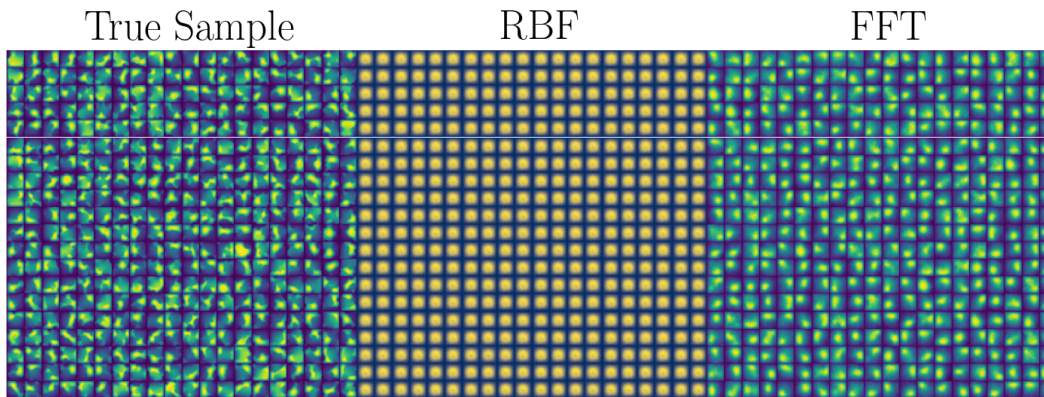


Figure 18: Generated 2D Darcy flow pressures, (Li et al., 2021), after 12,000 parameter updates using MLE / IS while adhering to KART. Radial Basis Functions, (RBFs) (Li, 2024), are contrasted against Fourier bases, (FFTs) (Xu et al., 2024), using lognormal latent priors. RBF is colored differently for clarity.

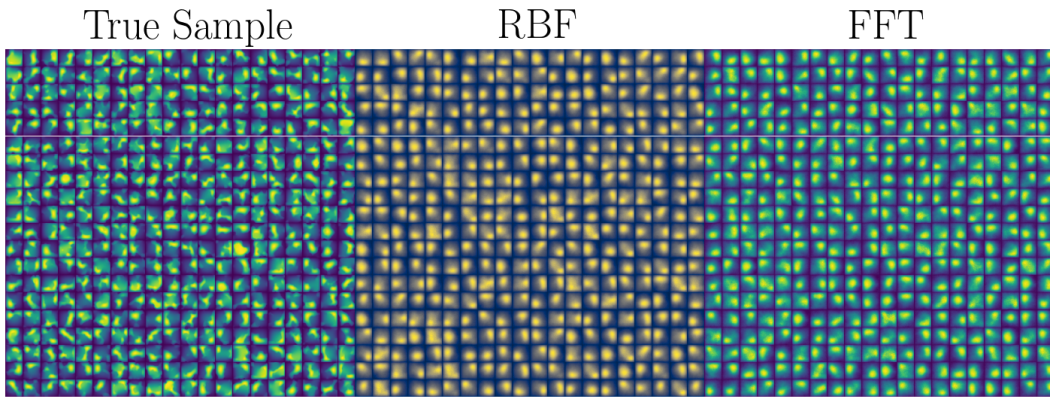


Figure 19: Generated 2D Darcy flow pressures, (Li et al., 2021), after 12,000 parameter updates using MLE / IS while adhering to KART. Radial Basis Functions, (RBFs) (Li, 2024), are contrasted against Fourier bases, (FFTs) (Xu et al., 2024), using uniform latent priors. RBF is colored differently for clarity.

A.7.4 SVHN



(a) SVHN with mixture prior and MLE

(b) SVHN with mixture prior and SE

Figure 20: Generated samples from T-KAM trained on SVHN using a mixture Chebyshev KAN prior, (SS et al., 2024), after 8,000 parameter updates with ITS prior and ULA posterior sampling.



(a) SVHN with deep prior and MLE

(b) SVHN with deep prior and SE

Figure 21: Generated samples from T-KAM trained on SVHN using a deep Chebyshev KAN prior, (SS et al., 2024), after 8,000 parameter updates with ULA prior and ULA posterior sampling.

A.7.5 CIFAR-10



(a) CIFAR-10 with mixture prior and MLE

(b) CIFAR-10 with mixture prior and SE

Figure 22: Generated samples from T-KAM trained on CIFAR-10 using a mixture Chebyshev KAN prior, (SS et al., 2024), after 8,000 parameter updates with ITS prior and ULA posterior sampling.

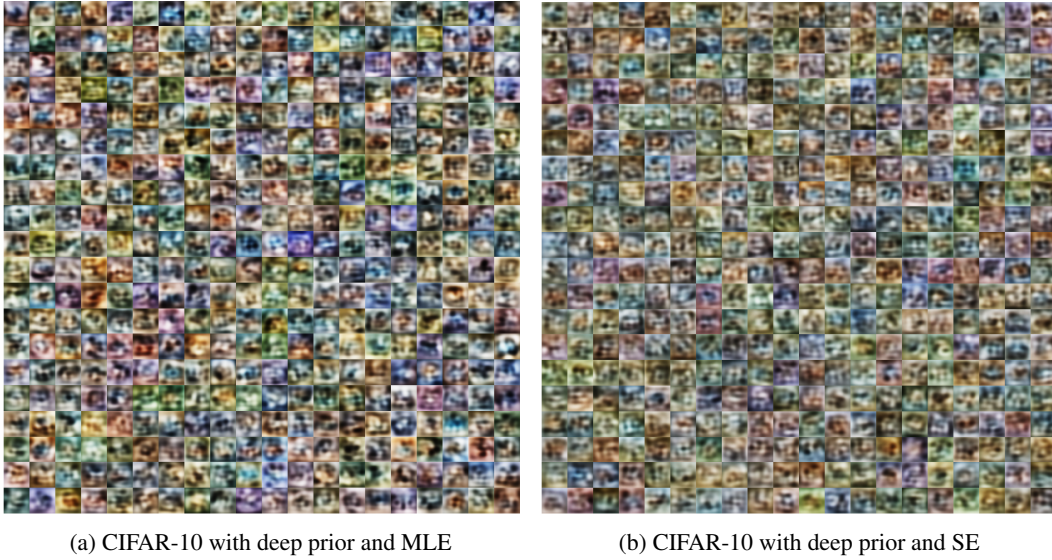


Figure 23: Samples from T-KAM trained on CIFAR-10 using a deep Chebyshev KAN prior, (SS et al., 2024), after 8,000 parameter updates with ULA prior and ULA posterior sampling.

A.8 TOP 3 EXTRACTED PRIORS

The following priors were extracted from trained T-KAM models, each corresponding to the first three components of prior $q = 1$.

A.8.1 MNIST RBF

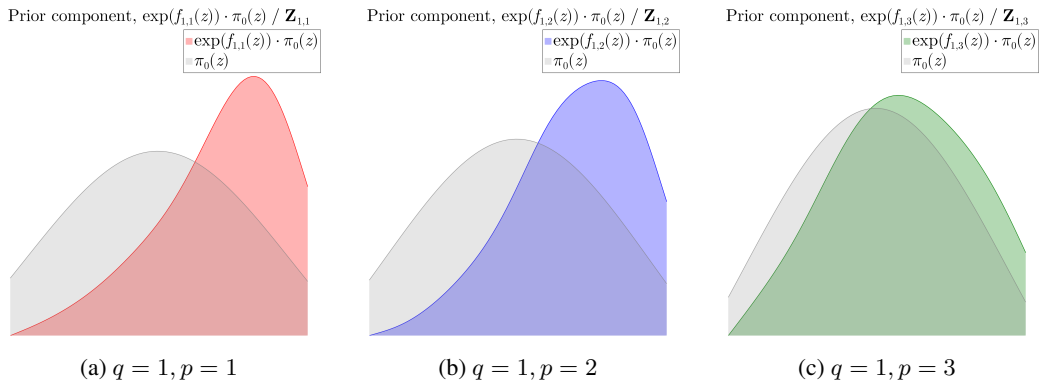


Figure 24: Three components from T-KAM's prior after training on MNIST for 2,000 parameter updates with RBF bases and Gaussian constrained priors.

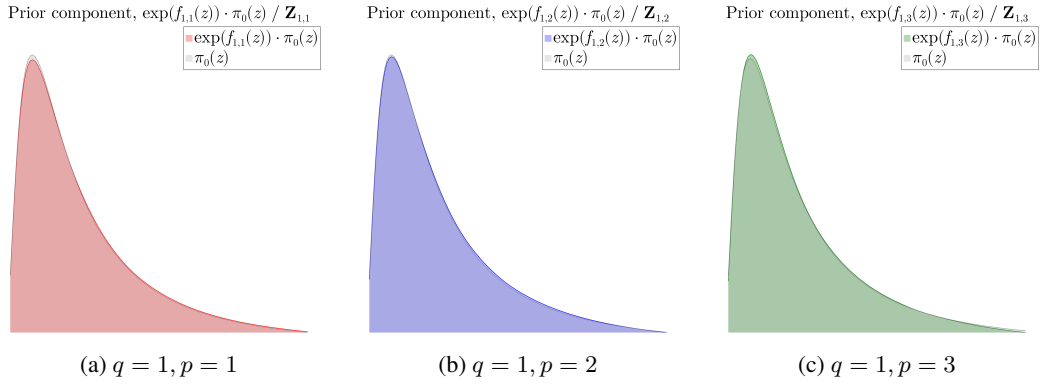


Figure 25: Three components from T-KAM's prior after training on MNIST for 2,000 parameter updates with RBF bases and lognormal constrained priors.

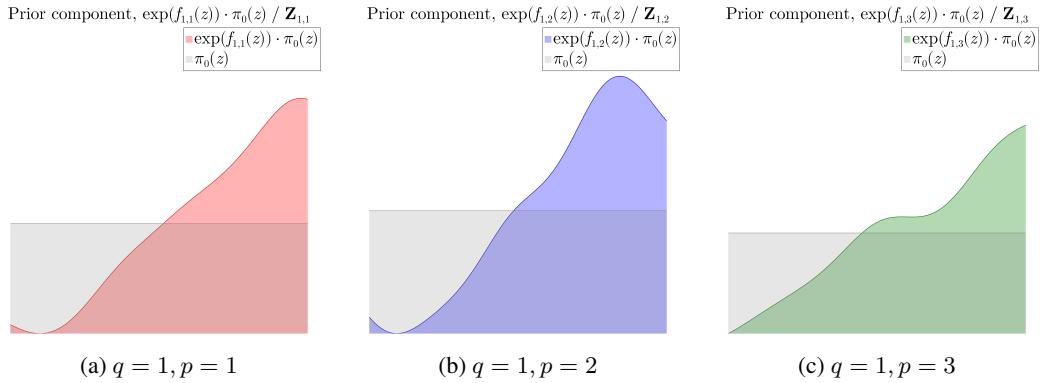


Figure 26: Three components from T-KAM's prior after training on MNIST for 2,000 parameter updates with RBF bases and uniform constrained priors.

A.8.2 MNIST FFT

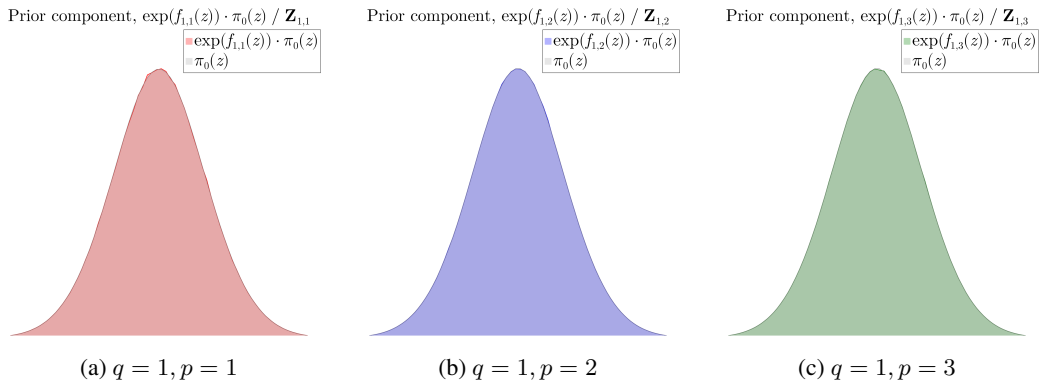


Figure 27: Three components from T-KAM's prior after training on MNIST for 2,000 parameter updates with FFT bases and Gaussian constrained priors.

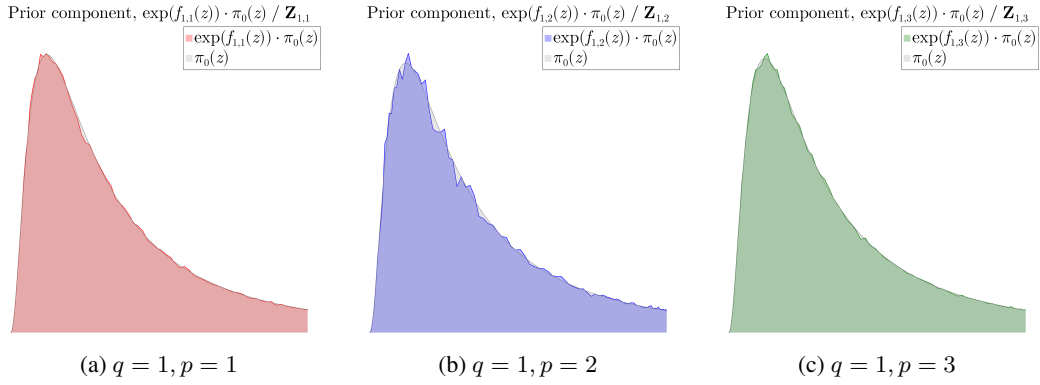


Figure 28: Three components from T-KAM's prior after training on MNIST for 2,000 parameter updates with FFT bases and lognormal constrained priors.

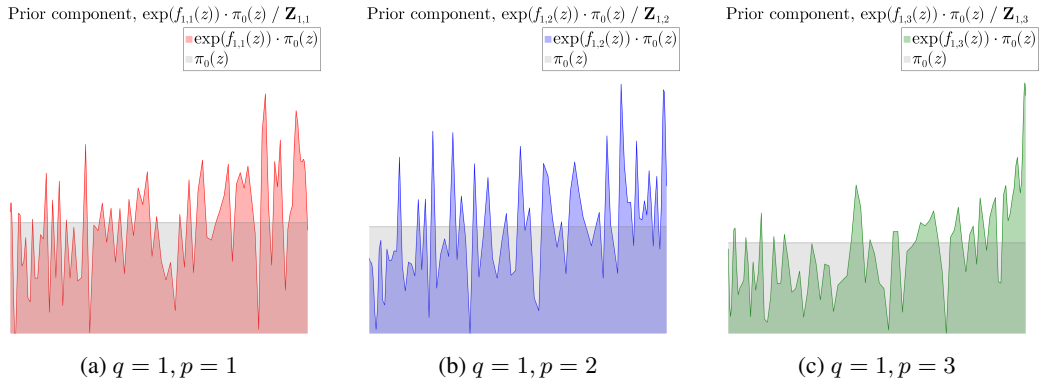


Figure 29: Three components from T-KAM's prior after training on MNIST for 2,000 parameter updates with FFT bases and uniform constrained priors.

A.8.3 FMNIST RBF

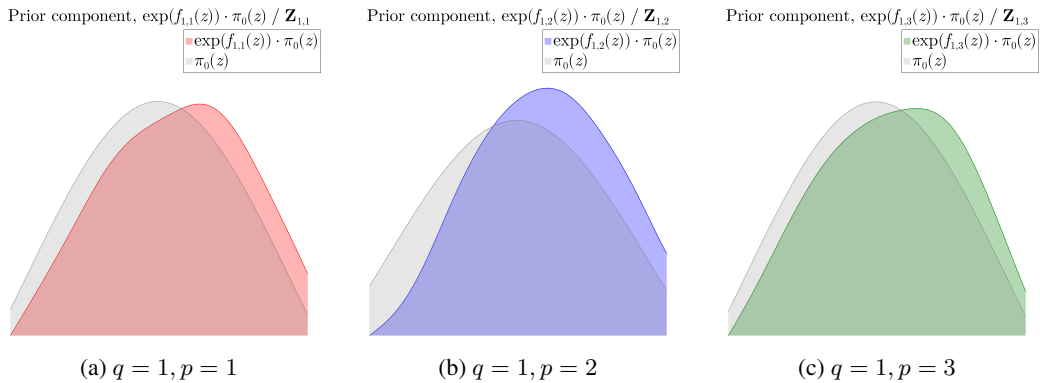


Figure 30: Three components from T-KAM's prior after training on FMNIST for 2,000 parameter updates with RBF bases and Gaussian constrained priors.

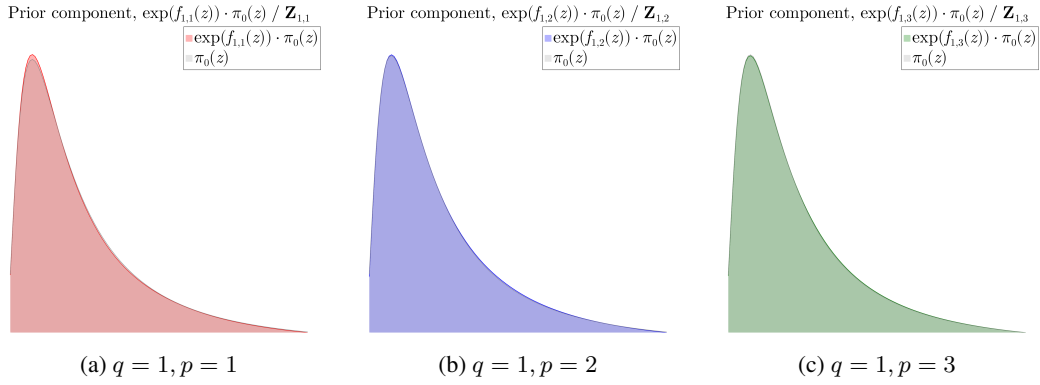


Figure 31: Three components from T-KAM's prior after training on FMNIST for 2,000 parameter updates with RBF bases and lognormal constrained priors.

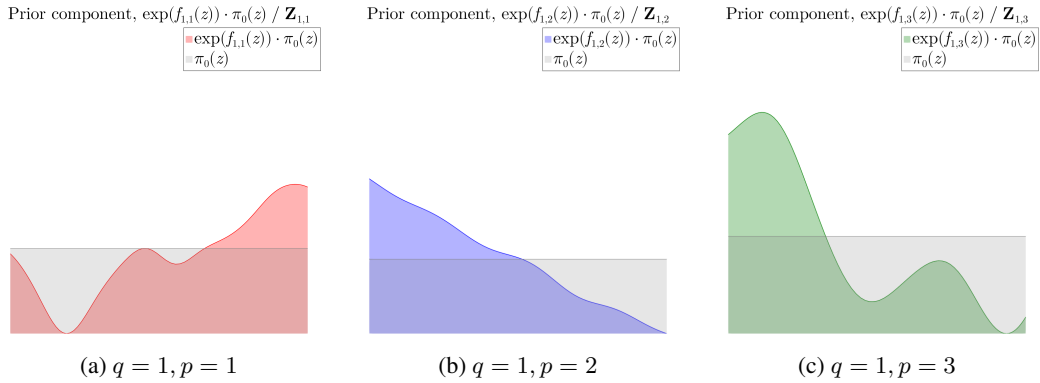


Figure 32: Three components from T-KAM's prior after training on FMNIST for 2,000 parameter updates with RBF bases and uniform constrained priors.

A.8.4 FMNIST FFT

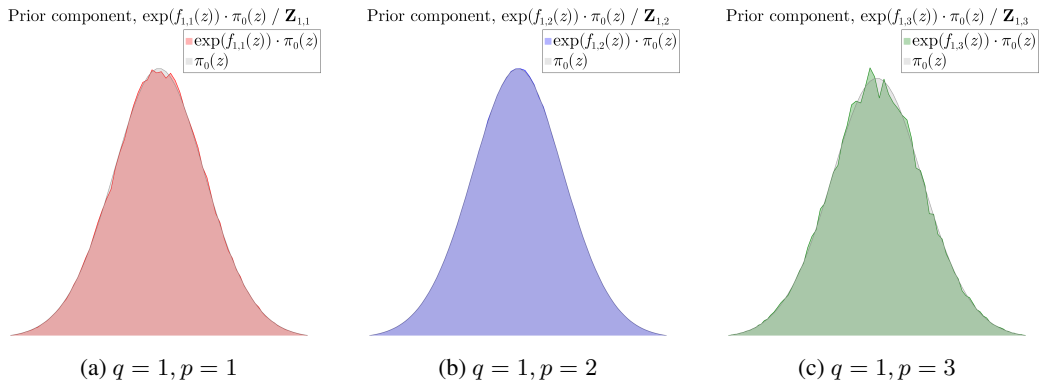


Figure 33: Three components from T-KAM's prior after training on FMNIST for 2,000 parameter updates with FFT bases and Gaussian constrained priors.

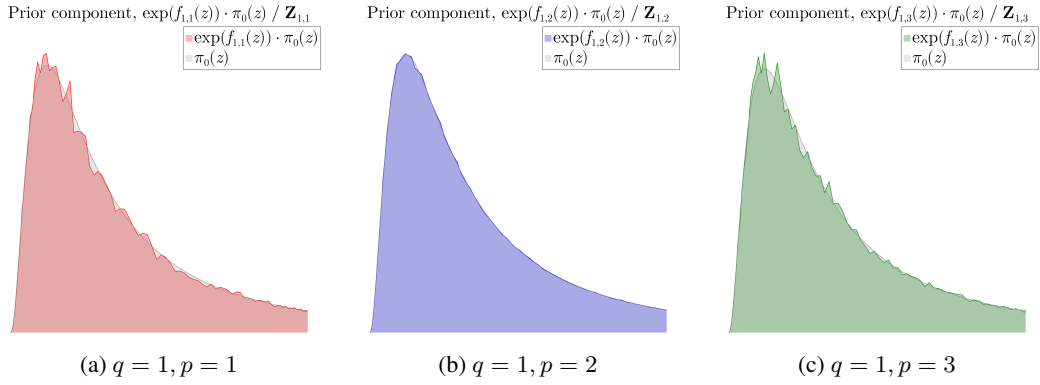


Figure 34: Three components from T-KAM's prior after training on FMNIST for 2,000 parameter updates with FFT bases and lognormal constrained priors.

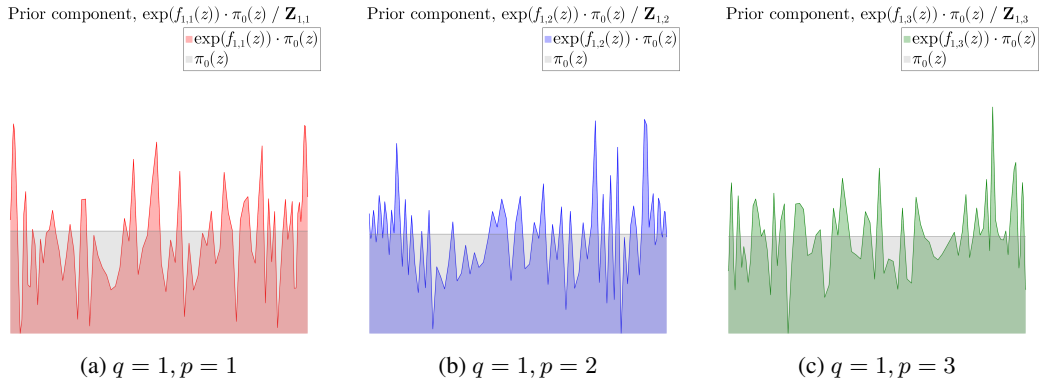


Figure 35: Three components from T-KAM's prior after training on FMNIST for 2,000 parameter updates with FFT bases and uniform constrained priors.

A.8.5 DARCY RBF

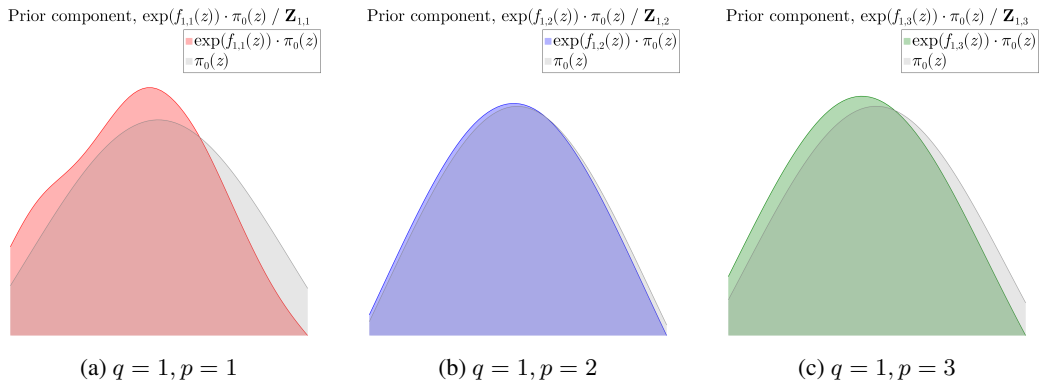


Figure 36: Three components from T-KAM's prior after training on Darcy flow pressures for 12,000 parameter updates with RBF bases and Gaussian constrained priors.

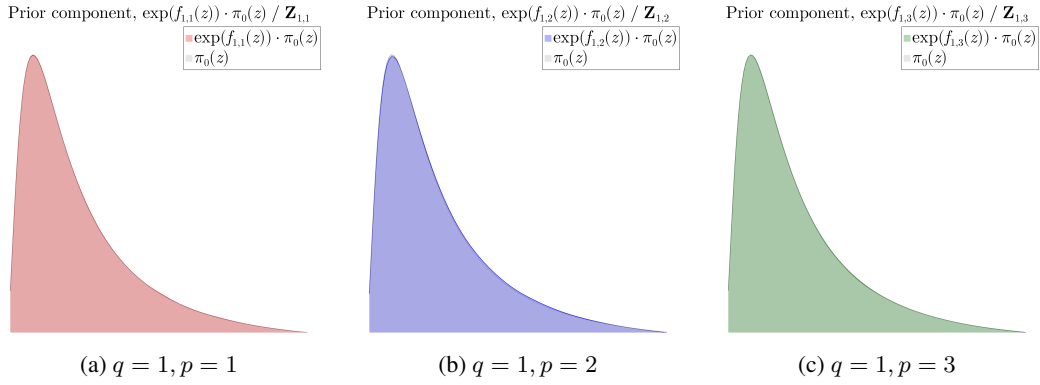


Figure 37: Three components from T-KAM's prior after training on Darcy flow pressures for 12,000 parameter updates with RBF bases and lognormal constrained priors.

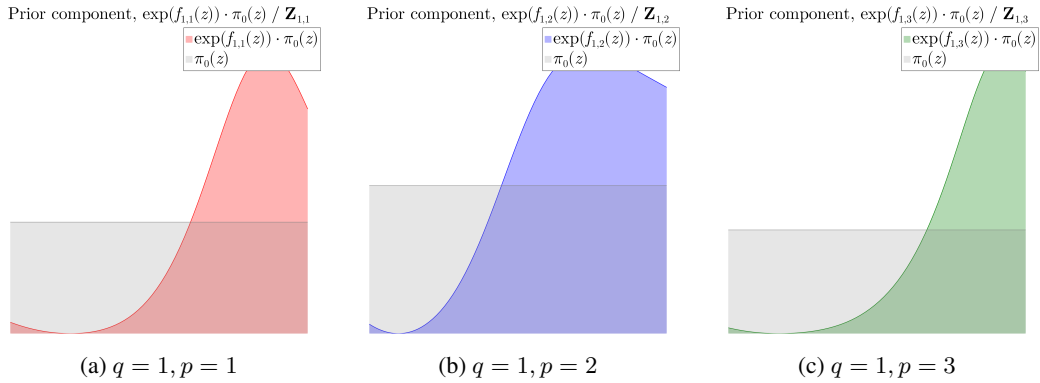


Figure 38: Three components from T-KAM's prior after training on Darcy flow pressures for 12,000 parameter updates with RBF bases and uniform constrained priors.

A.8.6 DARCY FFT

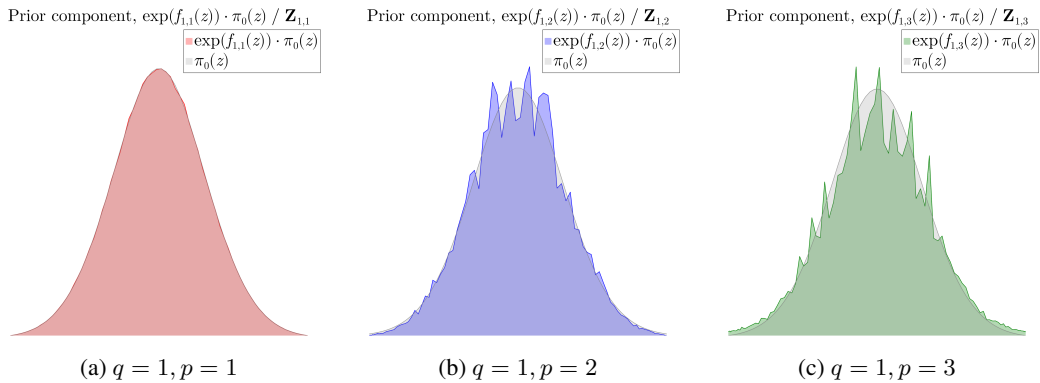


Figure 39: Three components from T-KAM's prior after training on Darcy flow pressures for 12,000 parameter updates with FFT bases and Gaussian constrained priors.

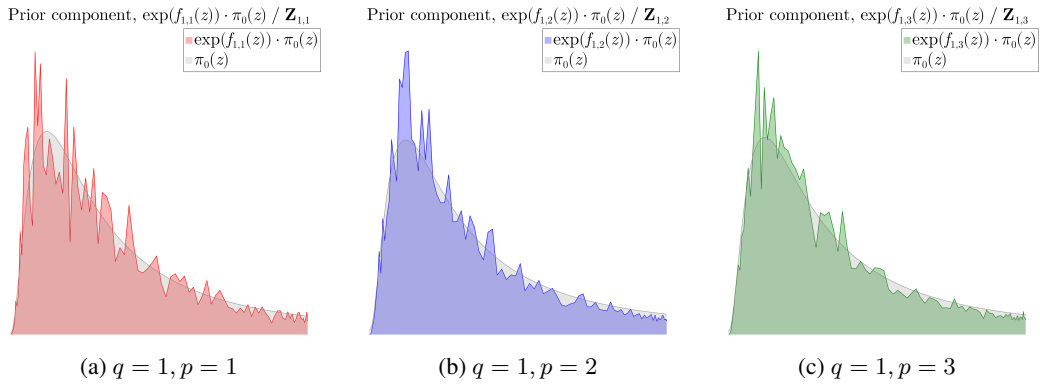


Figure 40: Three components from T-KAM's prior after training on Darcy flow pressures for 12,000 parameter updates with FFT bases and lognormal constrained priors.

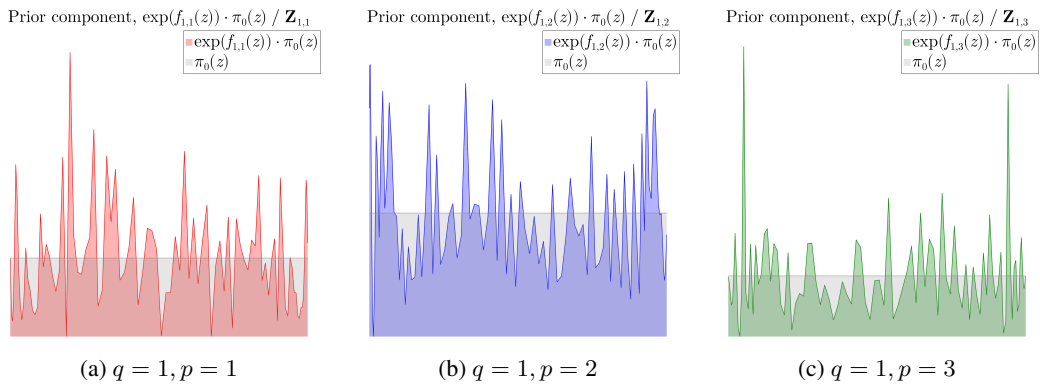


Figure 41: Three components from T-KAM's prior after training on Darcy flow pressures for 12,000 parameter updates with FFT bases and uniform constrained priors.